The Astrophysical Journal Supplement Series, 260:48 (29pp), 2022 June https://doi.org/10.3847/1538-4365/ac64f6
© 2022. The Author(s). Published by the American Astronomical Society.
OPEN ACCESS

Exploring γ-Ray Flares in the Long-term Light Curves of CTA 102 at GeV Energies

Xiongfei Geng[1,2,3], Nan Ding[4], Gang Cao[5], Yang Liu[2,3], Biwen Bao[2,3], Celine Chidiac[6], Pankaj Kushwaha[7,8,11], Zahir Shah[9], Zhijie Zhang[10], Xiongbang Yang[2,3], Tao Wen[2,3], Zejun Jiang[2,3], Li Zhang[2,3], Wei Zeng[2,3], Xiaohui Wu[2,3], Yao Qin[2,3], Meng Zhou[2,3], and Benzhong Dai[2,3,12]

[1] School of Electrical and Information Technology, Yunnan Minzu University, Kunming 650091, Yunnan, People's Republic of China; xiongfeigeng@ymu.edu.cn,
[2] School of Physics and Astronomy, Yunnan University, Kunming 650091, People's Republic of China; bzhdai@ynu.edu.cn
[3] Key Laboratory of Astroparticle Physics, Kunming 650091, People's Republic of China
[4] School of Physical Science and Technology, Kunming University, Kunming 650214, People's Republic of China; orient.dn@foxmail.com
[5] Department of Mathematics, Yunnan University of Finance and Economics, Kunming 650221, People's Republic of China
[6] Max-Planck-Institut für Radioastronomie (MPIfR), Auf dem Hügel 69, D-53121 Bonn, Germany
[7] Aryabhatta Research Institute of Observational Sciences (ARIES), Nainital 263002, India
[8] Department of Physical Sciences, Indian Institute of Science Education and Research Mohail, Knowledege City, Sector 81, SAS, Nagar, Punjab 140306, India
[9] Inter-University Center for Astronomy and Astrophysics, PB No. 4, Ganeshkhind, Pune-411007, India
[10] Department of Astronomy and Jiujiang Research Institute, Xiamen University, Xiamen 361005, People's Republic of China
Received 2020 May 26; revised 2022 January 22; accepted 2022 February 8; published 2022 June 23

Abstract

Blazar CTA 102 experienced an intense multiwavelength activity phase from 2015 to 2018; in particular, an unprecedented outburst was observed from 2016 October to 2017 February. In this work, we extract a 7 day binned γ-ray light curve from 2008 August to 2018 March in the energy range 0.1–300 GeV and identify three main outbursts. We study in detail the short-timescale variability of these three outbursts via an exponential function with parameterized rise and decay timescales. The obtained shortest rise and decay timescales are 0.70 ± 0.05 hr and 0.79 ± 0.27 hr, respectively. Based on these variability timescales, the physical parameters of the flaring region (e.g., the minimum Doppler factor and the emission region size) are constrained. The short-timescale flares exhibit a symmetric temporal profile within the error bars, implying that the rise and decay timescales are dominated by the light-crossing timescale or by disturbances caused by dense plasma blobs passing through the standing shock front in the jet region. We also find that the best-fitting form of the γ-ray spectra during the flare period is a power law with an exponential cutoff. The derived jet parameters from the spectral behavior and the temporal characteristics of the individual flares suggest that the γ-ray emission region is located upstream of the radio core. The extreme γ-ray flare of CTA 102 is likely to have been caused by magnetic reconnection.

Unified Astronomy Thesaurus concepts: Blazars (164); Gamma-rays (637); Active galactic nuclei (16); Relativistic jets (1390)

1. Introduction

Blazars, including BL Lac objects and flat-spectrum radio quasars (FSRQs), are a subclass of radio-loud active galactic nuclei (AGNs). Blazars possess distinctive observational characteristics, such as large amplitude, rapid variability, high and variable polarization, and compact radio emission (see, e.g., Urry & Padovani 1995; Padovani et al. 2017; Ding et al. 2019). The broadband electromagnetic radiation of blazars is dominated by nonthermal (NT) emission. Their spectral energy distributions (SEDs) typically exhibit two broad bumps: a low-energy bump between submillimeter and ultraviolet (UV)/X-rays and a high-energy bump at MeV–GeV energies. It is generally accepted that the low-energy component of these SEDs is caused by synchrotron emissions from relativistic electrons in the jet, whereas the mechanism of the high-energy component remains controversial. The high-energy component is usually explained by leptonic models (see, e.g., Finke et al. 2008; Böttcher et al. 2013; Cao & Wang 2013; Dermer et al. 2014; Ding et al. 2017, 2019; Xue et al. 2019; Zhang et al. 2020) or hybrid models, including leptonic and hadronic components (see, e.g., Cao & Wang 2014; Cerruti et al. 2015, 2019; Lewis et al. 2018, 2019; Cao et al. 2020). In terms of these aforementioned properties, constraining the nature of the high-energy emission arising from blazars has become an important objective for γ-ray astronomy (see, e.g., Burns et al. 2019; Murase & Bartos 2019; Rani et al. 2019).

Blazar variability has been studied extensively in attempts to reveal the nature of the NT radiation and the energy dissipation mechanisms of the relativistic jets. The variability timescales of blazars are divided into three categories: intraday variability, with timescales ranging from hours to days; short-term variability (STV), with timescales ranging from days to months; and long-term variability (LTV), with timescales ranging from months to years. Similarly, the variability timescales of blazar flares range from a few minutes to hours in the γ-ray band. Such extreme γ-ray flares reveal underlying physical information, such as the location and size of the emission region and the dynamics of the jet (see, e.g., Kushwaha et al. 2014a, 2014b; Nalewajko et al. 2014; Paliya 2015b; Ackermann et al. 2016; Ding et al. 2019). However, the exact mechanism(s) that leads to such extreme γ-ray flares is not fully understood. A variety of scenarios (see Aharonian et al. 2017 and Böttcher 2019a for recent reviews), such as shock-in-jet models (Böttcher & Dermer 2010; MAGIC Collaboration et al. 2018), magnetic reconnection events (Giannios 2013; Guo et al. 2014; Sironi et al. 2015;

[11] Aryabhatta Postdoctoral Fellow.
[12] Corresponding author.

Original content from this work may be used under the terms of the Creative Commons Attribution 4.0 licence. Any further distribution of this work must maintain attribution to the author(s) and the title of the work, journal citation and DOI.

Petropoulou et al. 2016; Morris et al. 2019), recollimation shock models (Bodo & Tavecchio 2018), and cloud-in-jet models (see, e.g., Barkov et al. 2012; Araudo et al. 2013; de la Cita et al. 2016; del Palacio et al. 2019) have been proposed to explain ultrafast γ-ray flares in blazars.

Blazar CTA 102 (4C+11.69, B2230+114, 4FGL J2232.6+1143) is classified as an FSRQ, with a redshift of $z \sim 1.037$ and a luminosity distance of ~6.9 Gpc (Chavushyan et al. 2020). The black hole mass is $M_{\rm BH} \sim 8.5 \times 10^8 M_\odot$ (Xiong & Zhang 2014; Zamaninasab et al. 2014). CTA 102 belongs to a class of optically violent variable quasars (Larionov et al. 2016; Raiteri et al. 2017), and is categorized as a highly polarized quasar (optical polarization >3%; Moore & Stockman 1981).

CTA 102 was first detected in the γ-ray band by the Energetic Gamma Ray Experiment Telescope on board the Compton Gamma Ray Observatory, at a level of $(2.4 \pm 0.5) \times 10^{-7}$ ph cm^{-2} s^{-1} ($E > 100$ MeV), corresponding to a γ-ray luminosity of $L_\gamma = 5 \times 10^{47}$ erg s^{-1} (Nolan et al. 1993). It is regularly detected by the Fermi Gamma-ray Space Telescope. At the beginning of Fermi's operation, the source was detected in a low-flux stage, with an average flux of $F_{>100\rm MeV} \sim 2 \times 10^{-7}$ ph cm^{-2} s^{-1}. In 2012, Larionov et al. (2016) reported that the source exhibited a significant γ-ray outburst, with a peak flux of $F_{>100\rm MeV} \sim 8 \times 10^{-6}$ ph cm^{-2} s^{-1}. The outburst was also detected at other frequencies, i.e., radio, optical, UV, near-infrared, and X-ray (see, e.g., Carrasco et al. 2012; Larionov et al. 2012; Casadio et al. 2015). Using multiwavelength data, Casadio et al. (2015) claimed that the location of the γ-ray emission region was located downstream of the radio core, on the scale of parsecs away from the black hole.

From 2015 to 2017, CTA 102 underwent an unprecedented outburst throughout all the observed electromagnetic wavebands (see, e.g., Ciprini & Verrecchia 2016; Ojha et al. 2017; Casadio et al. 2019; De et al. 2019). The duration of the outburst was close to four months, which encouraged some researchers to investigate its possible physical origin using multiwavelength data (see, e.g., Raiteri et al. 2017; Zacharias et al. 2017, 2019; Gasparyan et al. 2018; Kaur & Baliyan 2018; Casadio et al. 2019; D'Ammando et al. 2019). This long-term outburst has also been proposed as arising from the ablation of a gas cloud that possibly originated from the atmosphere of a red-giant star or a star-forming region that passed through the jet (Zacharias et al. 2017, 2019). Investigating this long-term outburst, Shukla et al. (2018) found that the source underwent a rapid γ-ray flare, with a flux halving time on the order of ~5 minutes (4.7σ). Such rapid γ-ray variability challenges the standard synchrotron self-Compton or external Compton (EC) scenarios. Shukla et al. (2018) argued that the observed fast γ-ray variability may be due to the dissipation of magnetic islands or protons in a collimated beam from the base of the jet encountering turbulent plasma at the end of the magnetic nozzle. On the other hand, Casadio et al. (2019) argued that interaction between a superluminal component and a recollimation shock could have triggered the multiwavelength flares.

Up to now, we still do not have a clear understanding of the origin of the multiwavelength flares from CTA 102, especially the source and location of the γ-ray emission region. We also note that the source exhibited three significant γ-ray outbursts after 2015. Although many studies have been conducted, a dedicated study of the evolution of the variability and spectra of these three additional outbursts has yet to be conducted. Indeed, studies of variability and spectra are an important step toward understanding the emission mechanism(s) responsible for the origin of these outbursts. Furthering our knowledge of the variability timescales of CTA 102 may also allow us to constrain the location of the γ-ray emission region.

Motivated by the strong outburst activity exhibited by CTA 102, we have systematically investigated the spectral and variability properties of the individual outbursts. Specifically, the STV and spectra from three outburst periods are analyzed in detail, to constrain the various jet parameters, explore the physical origin of these flares, and ascertain the physical properties of the emission regions. The remainder of this paper is organized as follows. In Section 2, we provide a brief description of the observations and the data reduction procedure. The characteristics of the γ-ray variability from CTA 102 are shown in Section 3, and the γ-ray spectra are presented in Section 4. The main results of this work are discussed in Section 5. Finally, a summary is given in Section 6.

2. Fermi-LAT Observations and Data Reduction

Fermi-LAT is a pair-conversion γ-ray telescope sensitive to photon energies from 20 MeV to more than 300 GeV. It surveys the whole sky every ~3 hr, with a field-of-view of ≃2.4 sr (Atwood et al. 2009). This configuration is highly capable of studying the short-timescale evolutions of γ-ray sources. Using the Fermi-LAT public data server,[13] we collected the γ-ray data for CTA 102 from 2008 August 4 to 2018 March 15 (MJD 54,682.66–58,210.90) in the 0.1–300 GeV energy range.

Following the standard analysis procedure,[14] we used the Fermi-LAT science tool version `ScienceTools v11r5p3` to analyze the data for CTA 102 with the `P8R3_SOURCE_V3` instrument response functions. Only photon-like events classified as `evclass` = 128 and `evtype` = 3 were selected within a circular region of interest (ROI) of 15° radius, centered on the location of CTA 102 (R.A. = 338.152, decl. = 11.731, J2000). The time interval was calculated using the recommended selection "(DATA_QUAL == 1) && (LAT_CONFIG == 1)." To remove the contamination from background γ-rays from Earth's limb, a zenith angle cut of ⩽90° was applied. In this analysis, we used "make4FGLxml.py" to obtain the input model file, with the isotropic background `iso_P8R3_SOURCE_V3_v1.txt`[15] and the galactic diffuse-emission model `gll_iem_v07.fits`. Considering that the target is very bright, we removed sources with TS < 4 to avoid problems of convergence for each `gtlike` run (the test statistic is defined as TS $= -2\ln(L_{\rm max,0}/L_{\rm max,1})$, where $L_{\rm max,0}$ is the maximum-likelihood value for a model without an additional source (the "null hypothesis") and $L_{\rm max,1}$ is the maximum-likelihood value for a model with the additional source at a specified location). The model file contained sources within ROI+10° from the target. The photon indices and normalization of the sources within 7° from the center of CTA 102 were left to vary freely during the likelihood fitting. In cases where the convergence of the fit was not optimal, we fixed the photon indices of the sources between 3°.5 and 7°. If the TS values of the sources were larger than 4, the normalization of all the sources within 7° from the center of the target was left to vary freely.

Fluxes and spectra with different timescales (7 days, 1 day, 12 hr, 6 hr, and 3 hr binnings) were obtained using an unbinned

[13] https://fermi.gsfc.nasa.gov/cgi-bin/ssc/LAT/LATDataQuery.cgi
[14] https://fermi.gsfc.nasa.gov/ssc/data/analysis/
[15] https://fermi.gsfc.nasa.gov/ssc/data/access/lat/BackgroundModels.html

likelihood method. For the 7 day binning, the normalizations of the Galactic diffuse and isotropic emission were left to vary freely; for the short-timescale variability (such as the 1 day, 12 hr, 6 hr, and 3 hr time bins), we fixed the normalizations of the Galactic diffuse and isotropic emission to the values obtained by the analysis of the weekly data in the same period.

Using the unbinned likelihood method, we performed spectral analyses using data from several epochs by fitting the γ-ray spectra in the energy range 0.1–300 GeV with power-law (PL), log-parabola (LP), broken-PL (BPL), and PL with an exponential cutoff (PLEC) models. Definitions of these models are given on the FSSC website.[16] We used values of $\mathrm{TS_{curve}} = 2(\log \mathcal{L}(\mathrm{LP/PLEC/BPL}) - \log \mathcal{L}(\mathrm{PL}))$ to estimate the significances of the spectral curvatures (Nolan et al. 2012).

3. Light Curves of CTA 102

In this section, we present the light curves of CTA 102 between 2008 and 2018. The source exhibited three high-activity periods (see Figure 1(a)): Flare-I, Flare-II, and Flare-III. Each point on the light curves (for weekly and monthly binned data) was obtained by integrating the spectra over the energy range 0.1–300 GeV. The peak fluxes of the three flares in the weekly binned light curves are larger than 5×10^{-6} ph cm^{-2} s^{-1}, which allowed us to explore the variable characteristics of the outbursts with short temporal resolutions (down to $\sim$3 hr).

3.1. Long-term γ-Ray Light Curves

The weekly and monthly binned γ-ray light curves of CTA 102 are shown in Figure 1(a). Based on a visual inspection, we divided the flux evolution into seven different flux states (see Figure 1(a) and Table 1). During the first four years, the source was essentially at a steady level, with a mean flux of $\sim(0.19 \pm 0.01) \times 10^{-6}$ ph cm^{-2} s^{-1}. The source remained in this state until 2012 March (MJD 56,000.00), which we have defined as a "low state." After this period, the source showed a moderate flux enhancement around MJD 57,342.66, defined here as a "plateau state" (see Tanaka et al. 2011). The average flux of the plateau state—($\sim$0.57 $\pm$ 0.01) $\times 10^{-6}$ ph cm^{-2} s^{-1}—was three times higher than that during the quiescent state.

After the plateau state, the source entered into a strong activity state from 2015 November to 2018 March, which we have defined as a "flare state." During this period, we define a "moderate flare" as one with a peak flux of $<4 \times 10^{-6}$ ph cm^{-2} s^{-1} in the 7 day binned light curves, including "Interflare-I" (MJD 57,516.66–57,676.88) and "Interflare-II" (MJD 57, 804.80–58,056.20); on the contrary, the state with a peak flux of $>4 \times 10^{-6}$ ph cm^{-2} s^{-1} is defined as a "high-flare state," including Flare-I (MJD 57,342.66–57,516.66, 2015 November 16–2016 May 8), Flare-II (MJD 57,676.88–57,804.80, 2016 October 15–2017 February 20), and Flare-III (MJD 58,056.20–58,192.66, 2017 October 30–2018 March 15). Their peak fluxes—$(5.25 \pm 0.13) \times 10^{-6}$ ph cm^{-2} s^{-1}, $(12.46 \pm 0.15) \times 10^{-6}$ ph cm^{-2} s^{-1}, and $(5.47 \pm 0.13) \times 10^{-6}$ ph cm^{-2} s^{-1}—occurred at MJDs 57,433.66, 57,748.66, and 58,119.66, respectively.

Using the `gtsrcprob` tool provided by the Fermi science package, we searched for high-energy photons ($E \geqslant 10$ GeV) having >95% probabilities of being associated with the source. These high-energy photons are shown in Figure 1(c), and we note that the majority of the high-energy photons were observed from MJD 57,676.88 to MJD 57,804.80 (Flare-II). The highest photon energy was 97.9 GeV, with a significance level of $>3\sigma$ at MJD 57,773.34, in agreement with the lack of detection at very high energy or similar.[17]

3.2. Identifying the Flares of CTA 102

In the 1 day and 12 hr binned light curves, some subflares were clearly seen during each outburst. To identify these flares, we adopted the Bayesian block algorithm (Scargle et al. 2013; Meyer et al. 2019; Geng et al. 2020), which is included in the `astropy.stats`[18] and `astroML` packages. Here, we directly adopted the Bayesian block (BB) algorithm from `astropy.stats` to recognize flares with a false alarm rate parameter of $p_0 < 0.001$ ($>3\sigma$). The durations of these identified flares ranged from a few days to two weeks. We define the time interval before a flare as the "preflare" period. The time intervals between two flares are referred to as "interflare" periods and the interval after the last flare is referred to as the "postflare" period. If the flux $F_{>100\mathrm{MeV}}$ was nearly constant, we defined the interval as a "low state" (see Figures 2–7).

3.3. Short-timescale γ-Ray Light Curves

To further study the temporal characteristics of each flare, we extracted their 3 hr binned light curves. We adopted the following function to fit the temporal profile of each peak component (Abdo et al. 2010a):

$$F(t) = 2\,F_0[e^{(T_0-t)/T_r} + e^{(t-T_0)/T_f}]^{-1}, \quad (1)$$

where T_0 is the (approximate) time of the peak value, T_r and T_f represent the rise and decay timescales of the flare, respectively, and F_0 is the flux at T_0. The time of the maximum of a flare (T_p) was calculated with the parameters of Equation (1) (Hayashida et al. 2015; Wierzcholska & Siejkowski 2016) as $T_\mathrm{p} = T_0 + \frac{T_\mathrm{r}T_\mathrm{f}}{T_\mathrm{f}+T_\mathrm{r}} \ln\left(\frac{T_\mathrm{f}}{T_\mathrm{r}}\right)$, where T_p is equal to T_0 when $T_r = T_f$.

The 3 hr and 6 hr binned light curves exhibited multiple peaks. To fit these peaks, the following functions with multiple components were used:

$$\begin{aligned} F(t) = {} & 2\,F_0[e^{(T_0-t)/T_r} + e^{(t-T_0)/T_f}]^{-1} \\ & + 2\,F_1[e^{(T_1-t)/T_{r1}} + e^{(t-T_1)/T_{f1}}]^{-1} \\ & + \cdots + F_c. \end{aligned} \quad (2)$$

Considering that statistical fluctuations tend to dominate at the very shortest timescales, we adopted the BB method to identify the 3 hr and 6 hr binned light curves with a false alarm rate parameter of $p_0 = 0.05$ (95%; see Figure A1 of Appendix A), which avoids possible biases in the results for the rise and decay timescales. Subsequent fitting was performed by fixing the maximum value of the flux of each peak component. We first adopted Equation (1) to fit each peak individually, with the corresponding best-fitting parameters of the function being obtained. Afterward, multiple peaks in the light curves were fitted simultaneously using Equation (2). While performing the simultaneous fits, the fitted parameters obtained from the individual peaks were taken as the initial parameters. To validate the fit of each period, we calculated the corresponding residuals between the data and the best-fitting model. Here, the residuals of

[16] https://fermi.gsfc.nasa.gov/ssc/data/analysis/scitools/source_models.html

[17] http://tevcat.uchicago.edu/

[18] https://docs.astropy.org/en/stable/apiastropy.stats.bayesian_blocks.html

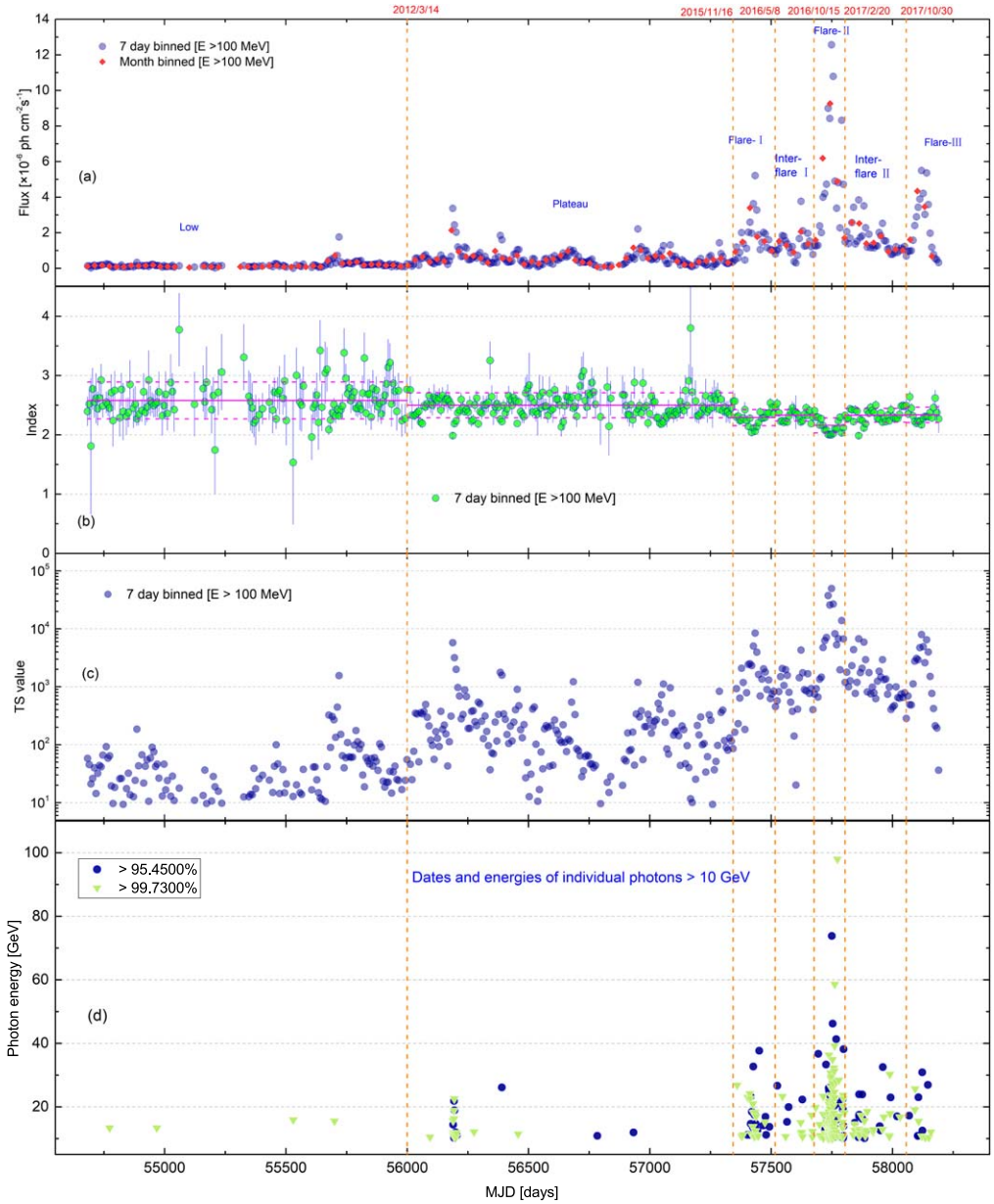

Figure 1. (a) Fermi-LAT light curve of CTA 102 from 2008 August to 2018 March at $E > 100$ MeV, with weekly binning (light blue circles) and monthly binning (red rectangles). The different patterns are divided by the vertical red dashed lines (see Table 1). (b) γ-ray photon index (Γ) as a function of time, with the horizontal magenta solid and dashed lines representing the averaged indices and their uncertainties, respectively. (c) Arrival times and energies of $E > 10$ GeV photons, with significance levels of 2σ and 3σ. (d) TS values (>9) as a function of time in logarithmic scale. The Gregorian calendar is added in the top panel, namely 2012 March 14–2017 October 30.

the fit have been taken as the ratio of the difference of the model and the observed flux to the flux error ((model flux−observed flux)/flux error).

We used $\xi = \frac{T_f - T_r}{T_f + T_r}$ to describe the symmetry of a flare, where $|\xi| < 1$. For a markedly symmetric flare, $|\xi| < 0.3$; for a moderately asymmetric flare, $0.3 < |\xi| < 0.7$; and for a markedly asymmetric flare, $0.7 < |\xi| < 1$. The best-fitting parameters are given in Table 2 and the fitted profiles are shown in Figures 3–6.

3.3.1. Variability of Flare-I

Figures 2(a) and (b) present the 1 day and 12 hr binned light curves of Flare-I. The source was initially in a stable state, which we have defined as the preflare period. Subsequently, three high-activity periods (Flare-Ia, Flare-Ib, and Flare-Ic) can clearly be seen between MJD 57,379.80–57,388.80 (2015 December 23–2016 January 1), MJD 57,423.80–57,433.80 (2016 February 5–2016 February 15), and MJD 57,433.80–57,445.80 (2016 February 15–2016 February 27), respectively. Their peak fluxes are larger than 6.0×10^{-6} ph cm^{-2} s^{-1}. An interflare state with a flux increase and a postflare state with a flux decrease were found during MJD 57,388.80–57,423.80 and MJD 57,445.80–57,457.80, respectively. After the postflare period, a low state was observed during MJD 57,457.80–57,516.80. Besides, we find that the maximum energy of the photons (37.7 GeV) occurred at MJD 57,450.79, with a 99.38% probability. In Flare-Ia, Flare-Ib, and Flare-Ic, the highest energies of the photons are 11.2 GeV, 32.7 GeV, and 16.9 GeV, with 99.88%, 98.63%, and 99.97% probabilities, respectively.

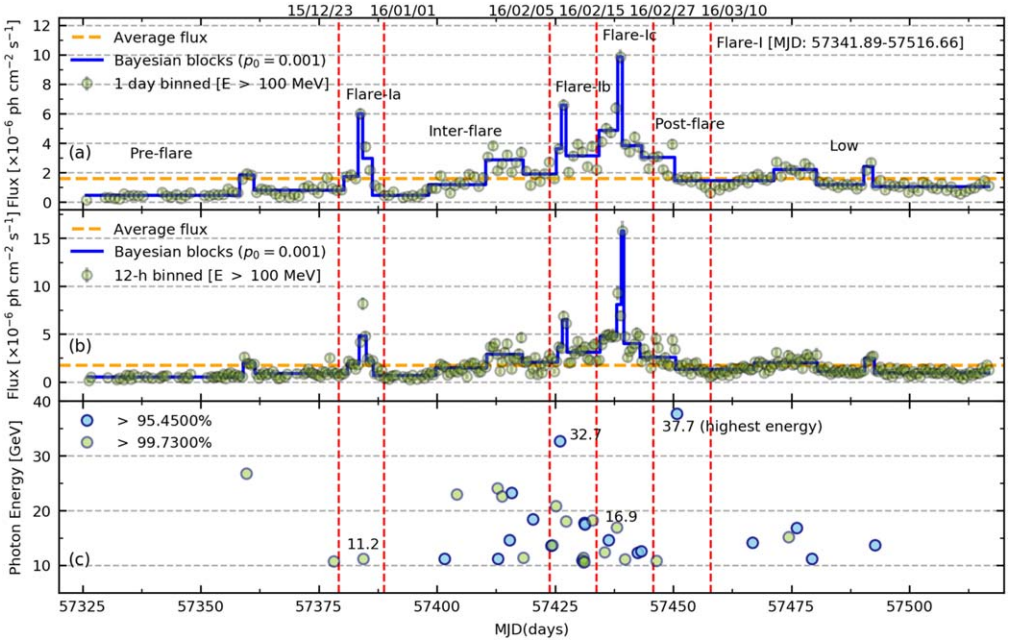

Figure 2. Panels (a) and (b) present the 1 day and 12 hr binned light curves of Flare-I above 100 MeV. The different episodes in the 1 day and 12 hr light curves are divided by the vertical red dashed lines. Three flares (Flare-Ia, Flare-Ib, and Flare-Ic) are highlighted. (c) Arrival times and energies of $E > 10$ GeV photons, with significance levels of $>2\sigma$ and $>3\sigma$. The Gregorian calendar is added in the top panel, namely 2015 December 23–2016 October 3.

Table 1
The Different States of CTA 102 Identified in Figure 1

Different States	Dates	MJD	Duration (yr)	Energy/Data (GeV)/MJD	R.A.	Decl.	Probability
Low	2008 Aug 4–2012 Mar 14	54,682.66–56,000.00	∼3.60	15.9 (55,530.41)	338.166	11.735	99.969%
Plateau	2012 Mar 14–2015 Nov 16	56,000.00–57,342.66	∼3.70	26.1 (56,390.25)	338.078	11.617	99.486%
Flare-I	2015 Nov 16–2016 May 8	57,342.66–57,516.66	∼0.48	37.7 (57,450.79)	338.259	11.696	99.375%
Interflare-I	2016 May 8–2016 Oct 15	57,516.66–57,676.88	∼0.44	26.6 (57,525.26)	338.096	11.817	99.643%
Flare-II	2016 Oct 15–2017 Feb 20	57,676.88–57,804.80	∼0.35	97.9 (57,773.34)	338.174	11.741	99.929%
Interflare-II	2017 Feb 20–2017 Oct 30	57,804.80–58,056.20	∼0.69	32.5 (57,960.07)	338.012	11.717	99.165%
Flare-III	2017 Oct 30–2018 Mar 15	58,056.20–58,192.66	∼0.37	30.9 (58,122.50)	338.097	11.546	98.262%

Note. Column 1 presents the different states of CTA 102 identified in Figure 1. Columns 2 and 3 are the time ranges of the different states. Column 4 is the duration of the different states. Column 5 presents the high-energy photons emitted during the different states, also including the times of the highest energies detected using Fermi-LAT. Columns 6 and 7 are the Galactic longitude and latitude, respectively, of the sources associated with the high-energy photons. The probabilities associated with these high-energy photons were calculated using the science tool `gtsrcprob`.

The 3 hr binned light curves of these three flares are shown in Figure 3. We find that Flare-Ia consists of two peaks (P1 and P2) at MJD $57{,}384.31 \pm 0.01$ and $57{,}385.06 \pm 0.03$, respectively; their peak fluxes are $(13.59 \pm 1.71) \times 10^{-6}$ ph cm^{-2} s^{-1} and $(4.84 \pm 1.34) \times 10^{-6}$ ph cm^{-2} s^{-1}, respectively (see Figure 3(a)). Flare-Ib and Flare-Ic include three peaks (P1, P2, and P3), and their peak fluxes are larger than 2.70×10^{-6} ph cm^{-2} s^{-1} (see Figures 3(c) and (e)). We also find that the decay timescales of the peaks in Flare-Ia are slightly longer than their rise timescales, and that the peaks exhibit symmetric temporal profiles. On the contrary, the rise timescales of the peaks during Flare-Ib and Flare-Ic are longer than their decay timescales (except for P3), and P3 shows a asymmetric temporal profile (see Table 2).

3.3.2. Variability of Flare-II

The 1 day and 12 hr binned light curves of Flare-II are shown in Figures 4(a) and (b). The light curves show seven variability patterns—a preflare period, Flare-IIa, Flare-IIb, Flare-IIc, and Flare-IId (2016 December 12–2017 January 10), an interflare period, and Flare-IIe. The preflare period includes two states: a low state (MJD 57,678.66–57,711.66) and a plateau period (MJD 57,711.66–57,734.66). The flux of the low state is below 4×10^{-6} ph cm^{-2} s^{-1}. An interflare period was observed between MJD 57,763.66 to 57,789.66, followed by Flare-IIe, which occurred from MJD 57,789.66–57,804.66 (2017 February 5–2017 February 20). We find that the flare states emitted most of the high-energy photons (above 10 GeV), and the maximum energies of the photons exceeded 30 GeV during all the identified flares (see Figure 4(c)).

Here, it is worth pointing out that the highest-energy photon for Flare-II is observed not during a peak flare, but during an interflare period. This is not inconsistent with the 7 day binned light curve. A flare is usually considered to be the result of the electrons in the jet being accelerated to higher energies. At subsequent times, the particles slowly cool, and the emitted flux starts to fall. In this process, the acceleration and cooling of the electrons are inhomogeneous. When the acceleration and cooling reach equilibrium, the electrons are accelerated to their

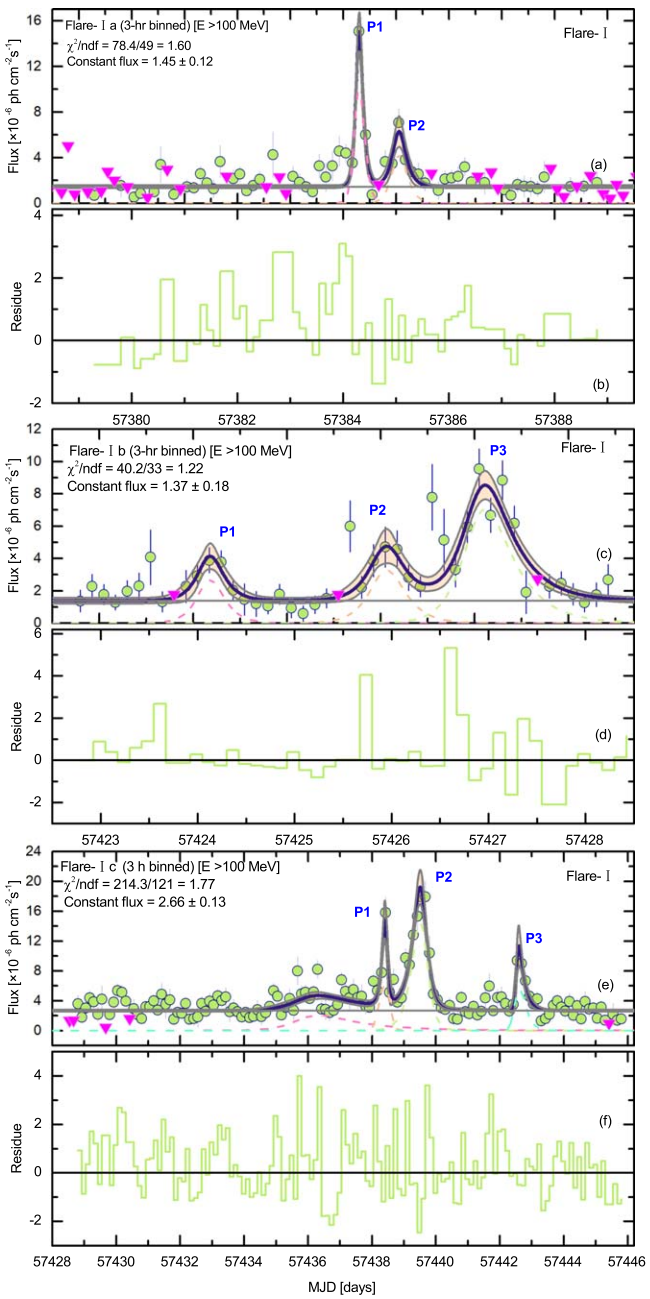

Figure 3. Panels (a), (c), and (e) present the 3 hr binned light curves of Flare-Ia, Flare-Ib, and Flare-Ic that were identified during Flare-I (see Figure 2). These light curves were fitted with Equation (2). Panels (b), (d), and (f) present the residuals of the model fit. The constant fluxes are shown in units of 10^{-6} ph cm^{-2} s^{-1}.

highest energies, implying that the highest energies do not necessarily occur during a peak flare, but may occur during an interflare period, in preparation for the next flare.

The 3 hr binned light curves of the flares are displayed in Figures 5(a)–(f) and 6(a)–(f). We find that Flare-IIa and Flare-IIc each consist of three distinctive peaks (P1, P2, and P3). The peak fluxes are $(8.74 \pm 1.22) \times 10^{-6}$ ph cm^{-2} s^{-1}, $(11.61 \pm 1.87) \times 10^{-6}$ ph cm^{-2} s^{-1}, and $(15.76 \pm 0.92) \times 10^{-6}$ ph cm^{-2} s^{-1} during Flare-IIa, and $(17.97 \pm 1.43) \times 10^{-6}$ ph cm^{-2} s^{-1}, $(12.26 \pm 4.47) \times 10^{-6}$ ph cm^{-2} s^{-1}, and $(12.16 \pm 1.25) \times 10^{-6}$ ph cm^{-2} s^{-1} during Flare-IIc. The observation period of Flare-IIb shows four distinctive peaks, P1, P2, P3, and P4, at MJD 57,741.41, 57,742.66, 57,744.78, and 57,746.68, with peak fluxes of $(4.87 \pm 0.60) \times 10^{-6}$ ph cm^{-2} s^{-1}, $(4.95 \pm 1.17) \times 10^{-6}$ ph cm^{-2} s^{-1}, $(7.78 \pm 0.71) \times 10^{-6}$ ph cm^{-2} s^{-1}, and $(4.47 \pm 1.59) \times 10^{-6}$ ph cm^{-2} s^{-1}, respectively. Two peaks, P1 and P2, were observed during Flare-IId (see Figure 6(a)), whose peak fluxes are $(9.56 \pm 2.58) \times 10^{-6}$ ph cm^{-2} s^{-1} on MJD 57,759.57 ± 0.05 and $(12.89 \pm 6.93) \times 10^{-6}$ ph cm^{-2} s^{-1} on MJD 57,760.29 ± 0.14. The larger error of the peak flux P2 may be attributed to statistical fluctuations in the very short timescales. For Flare-IIe, five peaks were clearly seen, and their peak fluxes all exceed 4.9×10^{-6} ph cm^{-2} s^{-1}. The modeling parameters are described in Table 2.

3.3.3. Variability of Flare-III

Similar to Flare-II, we extracted the 1 day and 12 hr binned light curves of Flare-III. The three flare periods, including Flare-IIIa (MJD 58,114.66–58,118.66), Flare-IIIb (MJD 58,118.66–58,139.66), and Flare-IIIc (MJD 58,140.66–58,149.66), can be seen in Figures 7(a) and (b). Two low states (Low 1 and Low 2) were observed from MJD 58,056.66 to 58,081.66 and from MJD 58,166.66 to 58,189.66, respectively; their averaged fluxes are 0.87×10^{-6} ph cm^{-2} s^{-1} and 0.61×10^{-6} ph cm^{-2} s^{-1}, respectively. A plateau state was observed from MJD 58,081.66 to 58,114.66. Only a few high-energy photons were detected during the Flare-III period. High-energy photons up to 30.9 GeV were detected at MJD 58,122.50, with a 98.26% probability (see Figure 7(c)). We also extracted the 3 hr binned light curve of Flare-IIIc, which shows three distinct peaks, with the maximum peak flux $(4.86 \pm 1.08) \times 10^{-6}$ ph cm^{-2} s^{-1} being observed at MJD 58,143.81 ± 0.05. Here, we do not study the short-timescale variability of Flare-IIIa and Flare-IIIb because they do not exhibit any sufficiently significant flare profiles in their 3 hr binned data. The modeling parameters are provided in Table 2.

3.4. Distribution Study of the Fluxes and Indices

3.4.1. Shapiro–Wilk Test

The continuous γ-ray observations provide a good opportunity to investigate the γ-ray flux distributions. The γ-ray fluxes from some blazars exhibit a log-normal distribution (see, e.g., Kushwaha et al. 2016, 2017; Shah et al. 2018; Ait Benkhali et al. 2019), which provides an important clue for understanding their γ-ray emission mechanism(s). To investigate the flux characteristics of CTA 102, Shapiro–Wilk (SW)[19] tests (see, e.g., Shapiro & Wilk 1965; Razali & Wah 2011) were performed. The SW test is a special module that can be used to conduct a normality test, which tests the null hypothesis (H_0) that the data are drawn from a normal distribution. The SW test estimates the hypothesis probability value (p-value), and if the p-value $\leqslant 0.05$, the null hypothesis is rejected, indicating deviation from the normality of the sample. If a normal distribution in the logarithmic flux scale is found, such distributions are known as log-normal.

The SW tests for Flare-I and Flare-II show that the p-values from the 1 day and 12 hr binned fluxes in log-scale are greater than 0.05, which indicates that the binned flux distributions are log-normal. For Flare-III, the p-values for the 1 day and 12 hr binned fluxes in linear-scale and log-scale are smaller than 0.05,

[19] https://docs.scipy.org/doc/scipy/reference/generated/scipy.stats.shapiro.html

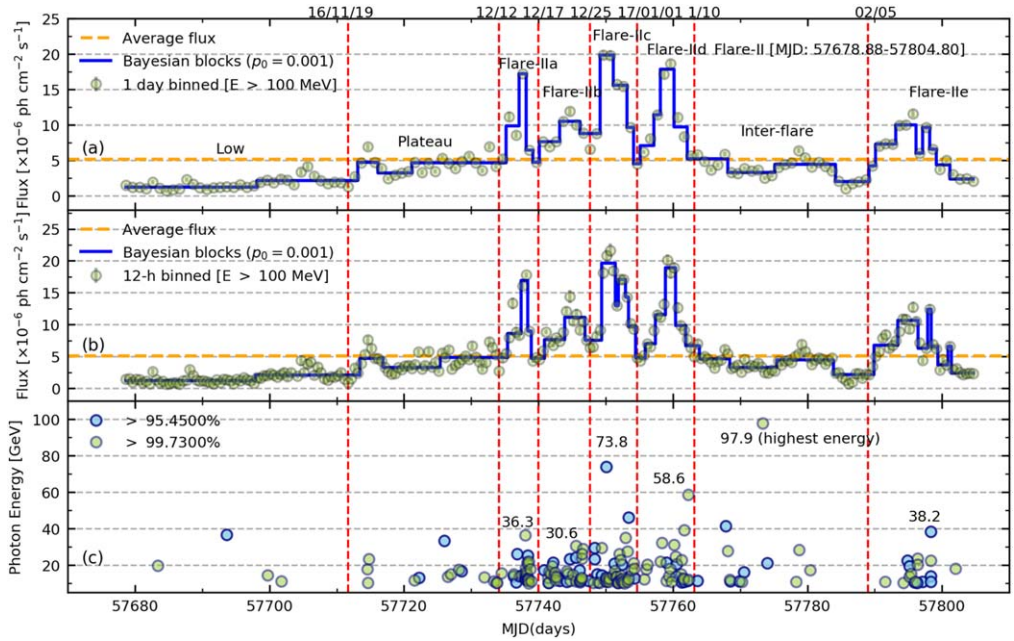

Figure 4. Panels (a) and (b) present the 1 day and 12 hr binned light curves of Flare-II above 100 MeV. The different episodes in the 1 day and 12 hr light curves are divided by the vertical red dashed lines. Five flares (Flare-IIa, Flare-IIb, Flare-IIc, Flare-IId, and Flare-IIe) are highlighted. (c) Arrival times and energies of $E > 10$ GeV photons, with significance levels of $>2\sigma$ and $>3\sigma$. The Gregorian calendar has been added in the top panel, namely 2016 November 19–2017 February 5.

suggesting that the binned flux distributions are non-normal or non-log-normal. Moreover, the p-values of the 1 day and 12 hr binned indices for Flare-I, Flare-II, and Flare-III suggest non-normal and non-log-normal distributions (see Table 3).

3.4.2. Histograms of the Fluxes

It is well known that histogram fitting is a helpful tool for exploring the nature of a distribution. Thus, we constructed histograms of the counts and normalized counts from the 1 day and 12 hr binned fluxes and indices in log-scale. In the cases of the 1 day and 12 hr binned fluxes from Flare-I, the counts and normalized counts exhibited a single peak. Thus, we fitted the flux histograms with the following probability density function (PDF):

$$f(x) = \frac{1}{\sqrt{2\pi\sigma}}\, e^{-\frac{(x-\mu)^2}{2\sigma^2}}, \tag{3}$$

where μ and σ are the centroid and width of the distribution, respectively. The best-fitting parameters are listed in Table 4 and the corresponding plots are shown in Figure 8 (left panels). The fitted parameters suggest that the 1 day and 12 hr binned flux distributions of Flare-I show a log-normal behavior, which is roughly consistent with the results obtained from the SW test statistic. On the contrary, the counts and normalized counts of the 1 day and 12 hr binned fluxes from Flare-II and Flare-III show a double-peaked structure. Hence, we further analyzed these distributions by fitting their histograms with a double-PDF function (Khatoon et al. 2020):

$$g(x) = \frac{a}{\sqrt{2\pi\sigma_1}}\, e^{-\frac{(x-\mu_1)^2}{2\sigma_1^2}} + \frac{1-a}{\sqrt{2\pi\sigma_2}}\, e^{-\frac{(x-\mu_2)^2}{2\sigma_2^2}}, \tag{4}$$

where a is the normalization fraction and μ_1 and μ_2 represent the centroids of the distribution with widths σ_1 and σ_2, respectively. In this work, the error of the normalization fraction "a" was not well constrained, due to poor data statistics in the flux histograms. Hence, we fixed the normalization fraction parameter "a" when fitting the flux histograms (empirically, the value of parameter "a" is obtained by testing different values). The best-fitting parameter values are provided in Table 5 and the corresponding plots are shown in Figures 8. The reduced χ^2 values suggest that the flux histograms from Flare-II and Flare-III are double log-normal, which is consistent with the results from the SW test statistic.

4. Time-resolved Spectra

4.1. γ-Ray Photon Index Evolution of the Flares

Spectral changes during the flare periods could potentially provide some important information regarding the dynamics, acceleration, and emission processes of the source. Figure 9 shows that the photon flux variations from Flare-I and Flare-III are characterized by a weak spectral hardening ($r_p < 0.5$ and $P < 10^{-5}$), while Flare-II shows a hint of spectral hardening as the source gets brighter, with $r_p \geqslant 0.5$ and $P < 10^{-10}$. Such behavior has already been observed from several blazars (e.g., PKS 1510-089, Abdo et al. 2010b; 3C 454.3, Ackermann et al. 2010) and radio galaxies (e.g., NGC 1275, Baghmanyan et al. 2017). A "harder-when-brighter" trend has also been reported for CTA 102 by considering 2 day intervals, with $r_p = -0.57$ and $P \ll 10^{-5}$ (Gasparyan et al. 2018).

4.2. Flux Correlation and Spectral Hysteresis

In this work, we further produced light curves in three energy bands: 0.1–1 GeV, 1–300 GeV, and 0.1–300 GeV. We found that the 3 hr binned light curves from each individual flare do not show a significant peak profile in the 1–300 GeV energy band, so we extracted 6 hr binned light curves for each individual flare, including Flare-Ia to Flare-Ic, Flare-IIa to Flare-IIe, and Flare-IIIc. We adopted the Bayesian block algorithm, with a false alarm rate parameter of $p_0 = 0.05$, to

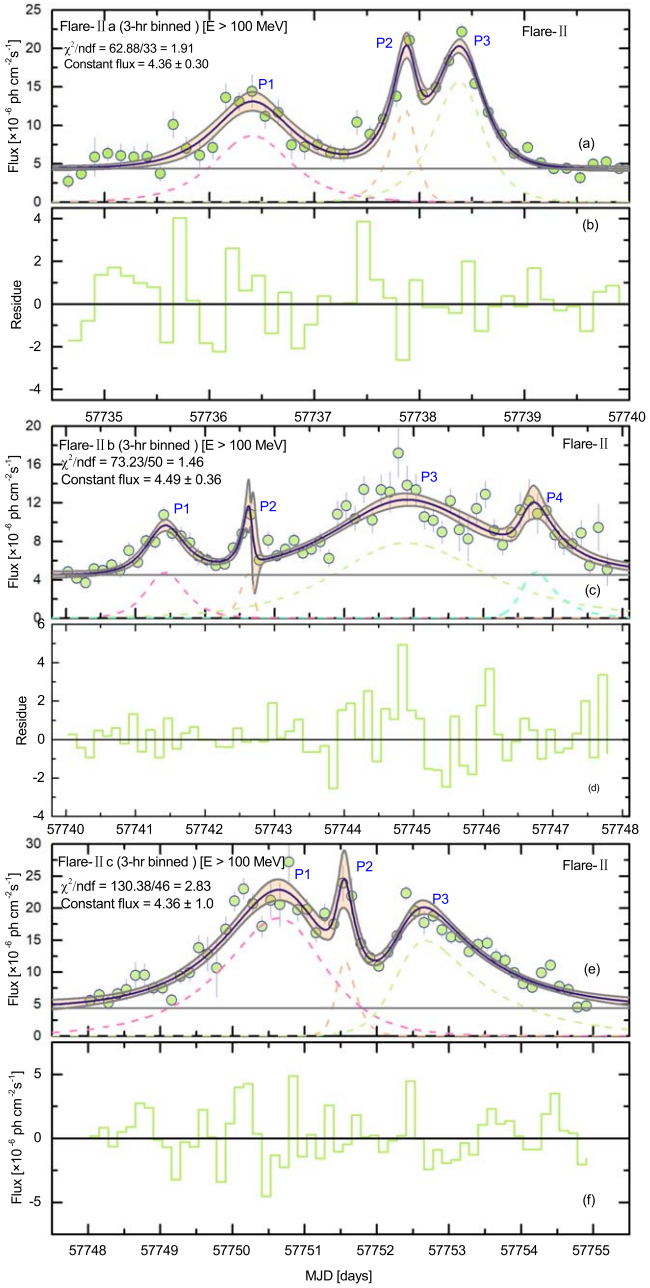

Figure 5. Panels (a), (c), and (e) present the 3 hr binned light curves of Flare-IIa, Flare-IIb, and Flare-IIc that were identified during Flare-II (see Figure 4). These light curves were fitted with Equation (2). Panels (b), (d), and (f) present the residuals of the model fit. The constant fluxes are shown in units of 10^{-6} ph cm^{-2} s^{-1}.

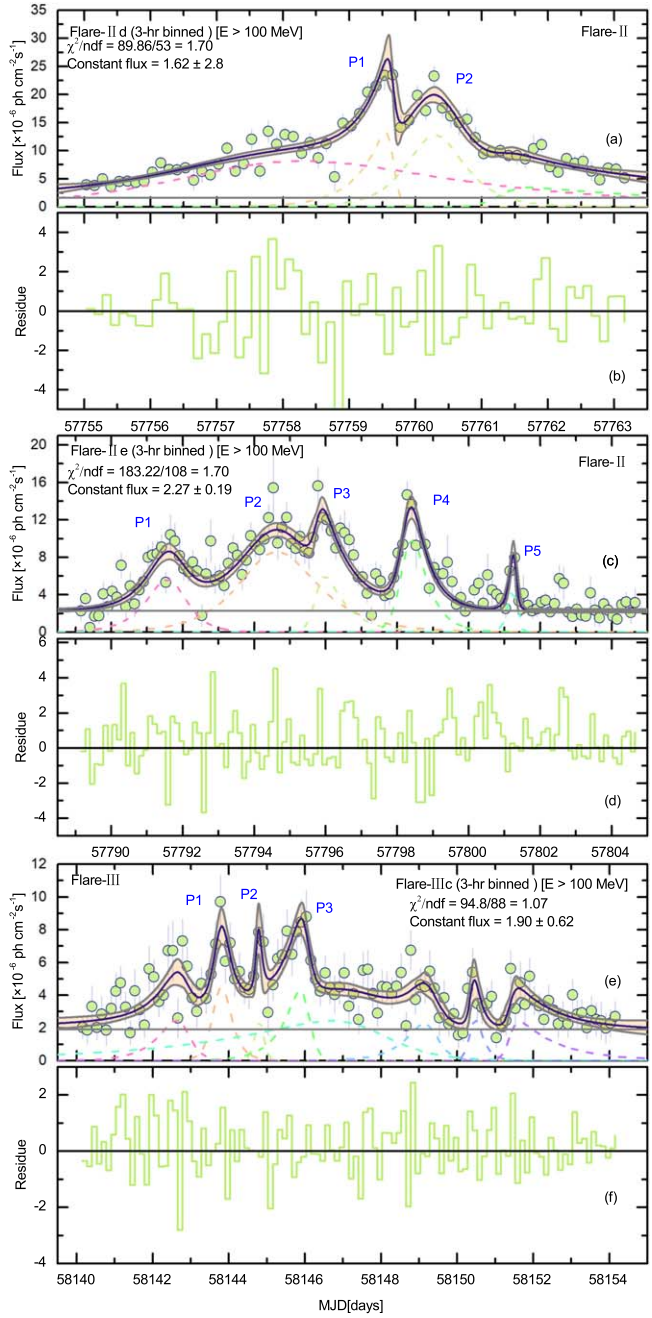

Figure 6. Panels (a) and (c) represent the 3 hr binned light curves of Flare-IId and Flare-IIe that were identified during Flare-II (see Figure 4). Panel (e) presents the 3 hr binned light curve of Flare-IIIc that was identified during Flare-III (see Figure 7). These light curves were fitted by Equation (2). Panels (b), (d), and (f) present the residuals of the model fit. The constant fluxes are shown in units of 10^{-6} ph cm^{-2} s^{-1}.

identify the peaks for the 6 hr binned light curves (see Figures B1 and B2 of Appendix B), and we fitted these light curves with Equation (2) (see Figures 10 and 11).

In the three energy bands (0.1–1 GeV, 1–300 GeV, and 0.1–300 GeV), we found that Flare-Ia and Flare-Ib exhibit a single peak, and that Flare-Ia has a symmetric temporal profile. Flare-Ic has two significant peaks in the 0.1–1 GeV and 0.1–300 GeV energy bands, where the highest peak fluxes are $(13.09 \pm 1.72) \times 10^{-6}$ ph cm^{-2} s^{-1} and $(15.12 \pm 2.26) \times 10^{-6}$ ph cm^{-2} s^{-1} at MJD 57,439.49 ± 0.02 and 57,439.48 ± 0.02, respectively. The period from Flare-IIa to Flare-IId shows seven peaks in the three energy bands. The highest peak fluxes of $(15.51 \pm 1.36) \times 10^{-6}$, $(2.45 \pm 0.27) \times 10^{-6}$, and $(18.59 \pm 1.59) \times 10^{-6}$ ph cm^{-2} s^{-1} were observed on MJD 57,750.66 ± 0.09, 57,750.33 ± 0.14, and 57,750.66 ± 0.08, respectively, all of which have a symmetric temporal profile. Flare-IIe shows three peaks in the three energy bands. Flare-IIIc has two peaks, P1 and P2, in the 0.1–1 GeV and 1–300 GeV energy bands. The details of the modeling parameters are provided in Tables 6–9. In Figure 11, it is clear that the light curve over the 0.1–300 GeV energy range is dominated by the emission in the 0.1–1 GeV range. A possible reason is the poor photon statistics in 1–300 GeV, with the shorter timescales, but we

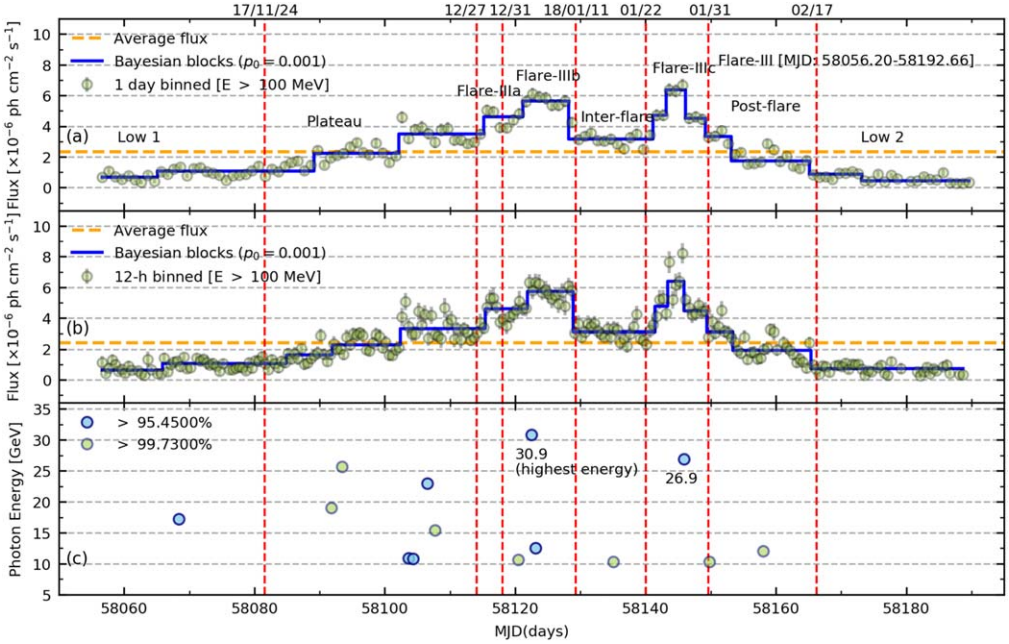

Figure 7. Panels (a) and (b) present the 1 day and 12 hr binned light curves of Flare-III above 100 MeV. The different episodes in the 1 day and 12 hr light curves are divided by the vertical red dashed lines. Three flares (Flare-IIIa, Flare-IIIb, and Flare-IIIc) are highlighted. (c) Arrival times and energies of $E > 10$ GeV photons, with significance levels of $>2\sigma$ and $>3\sigma$. The Gregorian calendar has been added in the top panel, namely 2017 November 24–2018 February 17.

also cannot rule out other possible causes, including a combination of different factors, such as jet dynamics, geometric effects in the emission region, the energy distribution of the particles therein, or moving emission regions in bent trajectories (see, e.g., Tanihata et al. 2001; Agudo et al. 2011; Kushwaha et al. 2014a, 2014b; Paliya 2015a, 2015b).

It has been shown that a "hard lag" should lead to a counterclockwise hysteresis loop, while a "soft lag" may result in a clockwise hysteresis loop (see, e.g., Abeysekara et al. 2017; Wang et al. 2018, 2019; Zhu et al. 2018). Motivated by this, we performed a time lag analysis to look for possible hints. The time lag analysis was performed using the discrete correlation function (DCF; see, e.g., Ding et al. 2019) between the different energy bands. The profile of the DCF as a function of time lag is approximated by a Gaussian distribution (Rani et al. 2013a), whose functional form is $\mathrm{DCF}(t) = A \times e^{\left(\frac{-(t-B)^2}{2C^2}\right)} + D$, where A is the DCF peak value above the background value D, B is the time lag, and C is the width of the Gaussian function. Figure 12 shows the DCF between the 0.1–1 GeV and 1–300 GeV energy bands. Considering the good photon statistics in the high-energy band, the 6 hr binned light curves of the flares were adopted in this analysis. Flare-Ia and Flare-Ib, Flare-IIa and Flare-IIb, and Flare-IIIa were not considered due to poor data statistics. No significant evidence was found for a time lag between the 0.1–1 GeV and 1–300 GeV energy bands.

To further confirm the above indications, we plotted the photon index as a function of flux for all of the identified flares, as displayed in Figures 13 and 14. Only panels (d) and (f) in Figure 13 exhibit a counterclockwise hysteresis loop, while panels (e), (g), and (h) exhibit a clockwise hysteresis loop. Such loops may be derived from particle acceleration via strong shocks and the cooling of radiating particles (Kirk et al. 1998; Baghmanyan et al. 2017). The physical mechanism responsible for the observed spectral evolution is very difficult to identify. The trajectory of a spectral evolution with either a clockwise or counterclockwise hysteresis loop depends on the total energy of the injected electrons and observed energy bands (see, e.g., Kirk & Mastichiadis 1999; Li & Kusunose 2000; Böttcher & Chiang 2002). For CTA 102, we did not find any consistent spectral hysteresis loops; hence, it is hard to draw a firm conclusion regarding the physical mechanism(s) producing the flare events based on spectral evolution alone.

4.3. SEDs of the Flares

Figure 15 shows the γ-ray spectra of the different states from the 7 day binned light curves. We find that the γ-ray spectra show a clear deviation from the PL model, and instead display curvature/cutoff/break features within the LP, PLEC, and BPL models. The significance levels of the spectral curvature/cutoffs/breaks are larger than 5σ (except during the low state; see Table 10). The cutoff energy found with the PLEC model for the different flux states is between 5.84 ± 0.51 and 14.86 ± 0.93 GeV, while the break energy found with the BPL model is between 2.21 ± 0.16 and 8.00 ± 0.59 GeV.

The same spectral models were also applied to the shorter time intervals (1 day binned light curves) of Flare-I, Flare-II, and Flare-III. The γ-ray spectra from these states are shown in Figures 16–18 and the corresponding best-fitting parameters are provided in Tables 11–13. These spectra again show a cutoff or break phenomenon. We find that the significance levels from the spectral cutoffs/breaks during the flare periods are larger than 4σ, except for Flare-Ia and Flare-Ib of the Flare-I period and Flare-IIIc of the Flare-III period. A possible reason for this could be the poorer photon statistics associated with the shorter timescales. We also find that the best-fitting form for the flare periods is the PLEC function, which is consistent with the results from Ballet et al. (2020; e.g., the Fermi Large Area Telescope Fourth Source Catalog, Data Release 2).

Progressive spectral hardening with increasing flux can be observed from the different states of the 7 day binned light curves. The spectral index (Γ) changes from 2.42 ± 0.03 to 1.98 ± 0.01 with the best-fitting function (see Figure 19(a)).

Table 2
Best-fitting Parameters of the 3 hr Binned Light Curves from the Flare Periods

	Peak	T_0 (MJD)	F_0 (10^{-6} ph cm^{-2} s^{-1})	T_r (day)	T_f (day)	ξ	T_p (MJD)
				Flare-I			
Flare-Ia	P1	57,384.30	13.59 ± 1.71	0.05 ± 0.01	0.07 ± 0.01	0.16 ± 0.12	57,384.31 ± 0.01
	P2	57,385.05	4.84 ± 1.34	0.10 ± 0.04	0.12 ± 0.04	0.09 ± 0.26	57,385.06 ± 0.03
Flare-Ib	P1	57,424.17	2.75 ± 0.78	0.11 ± 0.06	0.13 ± 0.06	0.08 ± 0.35	57,424.18 ± 0.04
	P2	57,426.05	3.34 ± 1.04	0.15 ± 0.06	0.18 ± 0.07	0.09 ± 0.28	57,426.06 ± 0.05
	P3	57,427.05	6.84 ± 0.81	0.17 ± 0.04	0.30 ± 0.05	0.28 ± 0.13	57,427.11 ± 0.03
Flare-Ic	P1	57,438.42	11.19 ± 2.50	0.09 ± 0.02	0.06 ± 0.03	−0.20 ± 0.26	57,438.41 ± 0.02
	P2	57,439.55	16.03 ± 2.24	0.23 ± 0.03	0.16 ± 0.02	−0.18 ± 0.09	57,439.52 ± 0.02
	P3	57,442.55	7.20 ± 2.29	0.04 ± 0.02	0.17 ± 0.05	0.62 ± 0.18	57,442.60 ± 0.01
				Flare-II			
Flare-IIa	P1	57,736.41	8.74 ± 1.22	0.32 ± 0.07	0.33 ± 0.07	0.02 ± 0.15	57,736.41 ± 0.05
	P2	57,737.91	11.61 ± 1.87	0.15 ± 0.03	0.07 ± 0.02	−0.36 ± 0.15	57,737.87 ± 0.01
	P3	57,738.41	15.76 ± 0.92	0.24 ± 0.04	0.18 ± 0.02	−0.14 ± 0.10	57,738.38 ± 0.02
Flare-IIb	P1	57,741.41	4.87 ± 0.60	0.23 ± 0.05	0.26 ± 0.06	0.06 ± 0.16	57,741.42 ± 0.04
	P2	57,742.66	4.95 ± 1.17	0.11 ± 0.03	0.03 ± 0.03	−0.57 ± 0.35	57,742.63 ± 0.01
	P3	57,744.78	7.78 ± 0.71	0.85 ± 0.10	1.10 ± 0.23	0.13 ± 0.12	57,744.90 ± 0.12
	P4	57,746.66	4.47 ± 1.59	0.12 ± 0.08	0.33 ± 0.14	0.47 ± 0.31	57,746.75 ± 0.05
Flare-IIc	P1	57,750.78	17.97 ± 1.43	0.79 ± 0.11	0.49 ± 0.15	−0.23 ± 0.16	57,750.64 ± 0.08
	P2	57,751.53	12.26 ± 4.47	0.08 ± 0.05	0.14 ± 0.05	0.27 ± 0.33	57,751.56 ± 0.03
	P3	57,752.41	12.16 ± 1.25	0.23 ± 0.05	0.98 ± 0.15	0.62 ± 0.08	57,752.68 ± 0.04
Flare-IId	P1	57,759.66	9.56 ± 2.58	0.43 ± 0.23	0.04 ± 0.04	−0.83 ± 0.18	57,759.57 ± 0.05
	P2	57,760.28	12.89 ± 6.93	0.37 ± 0.19	0.40 ± 0.21	0.04 ± 0.37	57,760.29 ± 0.14
Flare-IIe	P1	57,791.66	5.64 ± 0.86	0.58 ± 0.12	0.42 ± 0.13	−0.16 ± 0.18	57,791.58 ± 0.08
	P2	57,794.53	8.61 ± 0.73	0.89 ± 0.17	1.09 ± 0.35	0.10 ± 0.18	57,794.63 ± 0.19
	P3	57,795.78	4.90 ± 1.58	0.12 ± 0.10	0.64 ± 0.23	0.68 ± 0.24	57,795.95 ± 0.06
	P4	57,798.28	9.53 ± 1.09	0.19 ± 0.04	0.45 ± 0.06	0.41 ± 0.10	57,798.40 ± 0.02
	P5	57,801.28	5.55 ± 1.38	0.13 ± 0.04	0.06 ± 0.04	−0.37 ± 0.32	57,801.25 ± 0.02
				Flare-III			
Flare-IIIc	P1	58,143.78	4.86 ± 1.15	0.17 ± 0.06	0.23 ± 0.08	0.15 ± 0.24	58,143.81 ± 0.05
	P2	58,144.78	3.74 ± 1.59	0.06 ± 0.04	0.07 ± 0.06	0.08 ± 0.54	58,144.78 ± 0.04
	P3	58,146.03	3.69 ± 0.93	0.50 ± 0.20	0.12 ± 0.06	−0.61 ± 0.20	58,145.89 ± 0.05

Note. These flares, including flares a–c from Flare-I, flares a–e from Flare-II, and flare c from Flare-III, are highlighted in Figures 2–7. The fitted 3 hr binned light curves are exhibited in Figures 3–6.

Table 3
SW Test Results for the 1 day and 12 hr Binned Flux/Index Distributions of Flare-I, Flare-II, and Flare-III

Activity Period	Time Bins	Number of Data Points	Log-normal (flux) SW (p-value)	Normal (flux) SW (p-value)	Log-normal (index) SW (p-value)	Normal (index) SW (p-value)
Flare-I	1 day	185	1.00(0.95)	0.79($<1\times10^{-3}$)	0.98(6×10^{-3})	0.95($<1\times10^{-3}$)
	12 hr	340	1.00(0.69)	0.71 ($<1\times10^{-3}$)	0.97($<1\times10^{-3}$)	0.93($<1\times10^{-3}$)
Flare-II	1 day	127	0.99(0.22)	0.83($<1\times10^{-3}$)	0.96($<1\times10^{-3}$)	0.94($<1\times10^{-3}$)
	12 hr	252	0.99(0.04)	0.83($<1\times10^{-3}$)	0.92($<1\times10^{-3}$)	0.88($<1\times10^{-3}$)
Flare-III	1 day	133	0.96($<1\times10^{-3}$)	0.91($<1\times10^{-3}$)	0.97(2×10^{-3})	0.94($<1\times10^{-3}$)
	12 hr	249	0.96($<1\times10^{-3}$)	0.92($<1\times10^{-3}$)	0.97($<1\times10^{-3}$)	0.94($<1\times10^{-3}$)

Note. Column 1: period of selected activity; Column 2: time bins; Column 3: number of data points; Columns 4 and 5: SW statistics of the flux and logarithmic flux distributions; and Columns 6 and 7: SW statistics of the index and logarithmic index distributions.

A significant amount of spectral hardening is also found in the Flare-I, Flare-II, and Flare-III periods with the 1 day binned light curves (see Figures 19(b)–(d)), and the spectral indices in the short intervals change from 2.21 ± 0.03 to 1.94 ± 0.03, 2.23 ± 0.04 to 1.86 ± 0.02, and 2.39 ± 0.07 to 2.03 ± 0.04 with the best-fitting function (the PLEC model), respectively. Similar behavior has been seen for other bright Fermi blazars, like 3C 279, S5 0836-71, 3C 454.3, PKS 1510-089, and PKS 1502+106 (e.g., Paliya 2015a, 2015b; Britto et al. 2016; Prince et al. 2017; Ding et al. 2019).

5. Discussion

We used 10 yr of Fermi-LAT observations to probe the high-energy emission properties of the FSRQ CTA 102. The motivations of this study were: (i) to investigate both the

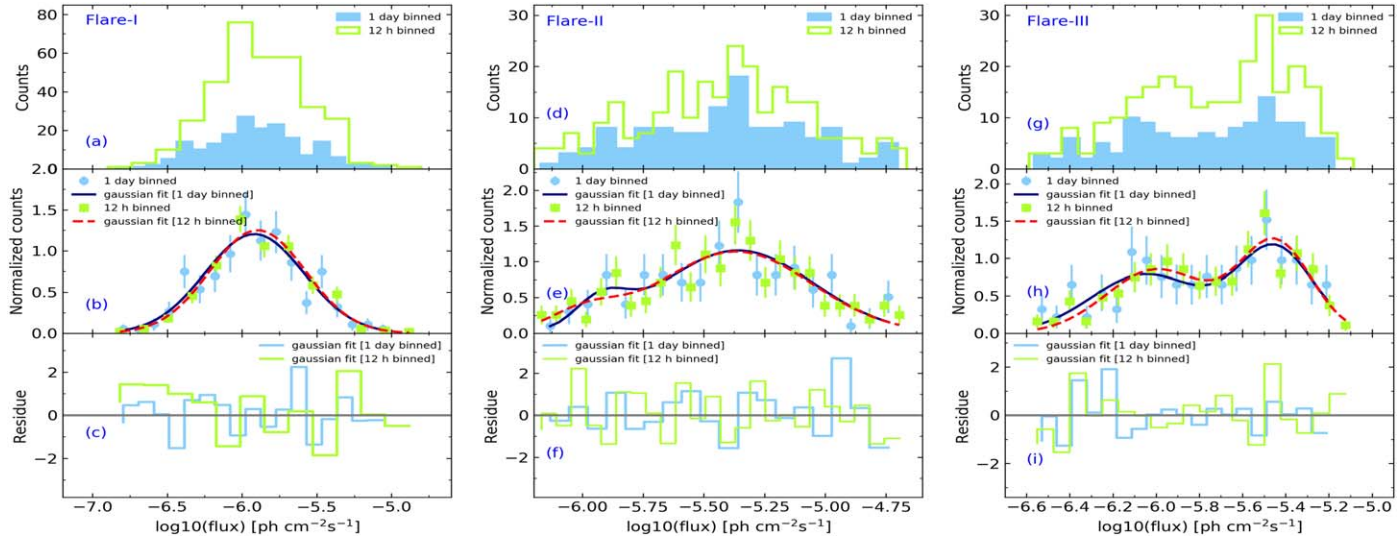

Figure 8. Flux distribution of CTA 102 in the γ-ray band. The left panels, (a), (b), and (c), present the counts, normalized counts, and residuals from the 1 day and 12 hr binned fluxes of Flare-I. The middle panels, (d), (e), and (f), present the counts, normalized counts, and residuals from the 1 day and 12 hr binned fluxes of Flare-II. The right panels, (g), (h), and (i), present the counts, normalized counts, and residuals from the 1 day and 12 hr binned fluxes of Flare-III. The sky blue lines show Gaussian fits to the normalized counts from the 1 day binned fluxes, and the red dashed lines display Gaussian fits to the normalized counts from the 12 hr binned fluxes.

Table 4
Best-fitting Parameter Values from Fitting Equation (3) to the Logarithmic Flux and Index Histograms

	Number of Bins	σ	μ	χ^2/ndf
		Flare-I (log10(flux))		
1 day	18	0.33 ± 0.02	-5.92 ± 0.02	$13.63/16 = 0.85$
12 hr	13	0.32 ± 0.01	-5.89 ± 0.02	$17.12/11 = 1.56$

Note. Column 2: number of bins in the distributions; Columns 3 and 4: best-fitting values of σ and μ, respectively; and Column 6: reduced χ^2/degrees of freedom.

Table 5
Best-fitting Parameter Values from Fitting Equation (4) to the Double Logarithm of the Fluxes

	Number of Bins	a	σ_1	μ_1	σ_2	μ_2	χ^2/ndf
			Flare-II (log10(flux))				
1 day	19	0.1	0.16 ± 0.07	-5.88 ± 0.07	0.27 ± 0.03	-5.33 ± 0.04	$18.11/15 = 1.21$
12 hr	25	0.1	0.15 ± 0.07	-5.99 ± 0.09	0.31 ± 0.02	-5.37 ± 0.03	$25.15/21 = 1.20$
			Flare-III (log10(flux))				
1 day	20	0.5	0.25 ± 0.03	-6.04 ± 0.04	0.18 ± 0.02	-5.45 ± 0.02	$11.64/16 = 0.73$
12 hr	20	0.5	0.23 ± 0.03	-6.00 ± 0.03	0.16 ± 0.02	-5.45 ± 0.02	$16.18/16 = 1.01$

Note. Column 2: number of bins in the distributions; Columns 3–8: best-fitting values of σ_1, μ_1, σ_2, and μ_2, respectively; and Column 9: reduced χ^2/degrees of freedom.

STV and LTV of the source; (ii) to probe its spectral variations; and (iii) to pinpoint the location and origin of the observed γ-ray flares in the source by estimating the jet parameters—the Doppler factor, the jet opening angle, the magnetic field in the emission region, the size of the emission region, the distance of the emission region from the central black hole, and the jet power of each flare.

5.1. γ-Ray Doppler Factor δ_γ

High-energy γ-ray photons can interact with softer photons to produce $e^{\pm}$ pairs. The cross section of this process is maximized by collisions between γ-rays of energy ϵ and ambient photons of energy $1/\epsilon$, where ϵ equals $\sim \sigma_T/5$ and σ_T is the Thomson scattering cross section (Svensson 1987). The importance of this process can be measured by the corresponding optical depth. If the optical depth is $\tau_{\gamma\gamma} < 1$, this leads to a lower limit on δ (see, e.g., Dondi & Ghisellini 1995; Finke et al. 2008; Ding et al. 2019):

$$\delta_{\min} \cong \left[\frac{(1+z)^2 \sigma_T d_L^2}{4 t_{\rm var} m_e c^4} \epsilon f_{\epsilon^{-1}} \right]^{\frac{1}{6}}, \quad (5)$$

where $d_L = 6.9$ Gpc is the luminosity distance of CTA 102; $t_{\rm var}$ is the observed variability timescale in units of seconds, which is approximately equal to $ln2 \times T_f$ (see, e.g., Paliya 2015a; Ding et al. 2019); $\epsilon = E/(m_e c^2)$ is the dimensionless energy of a

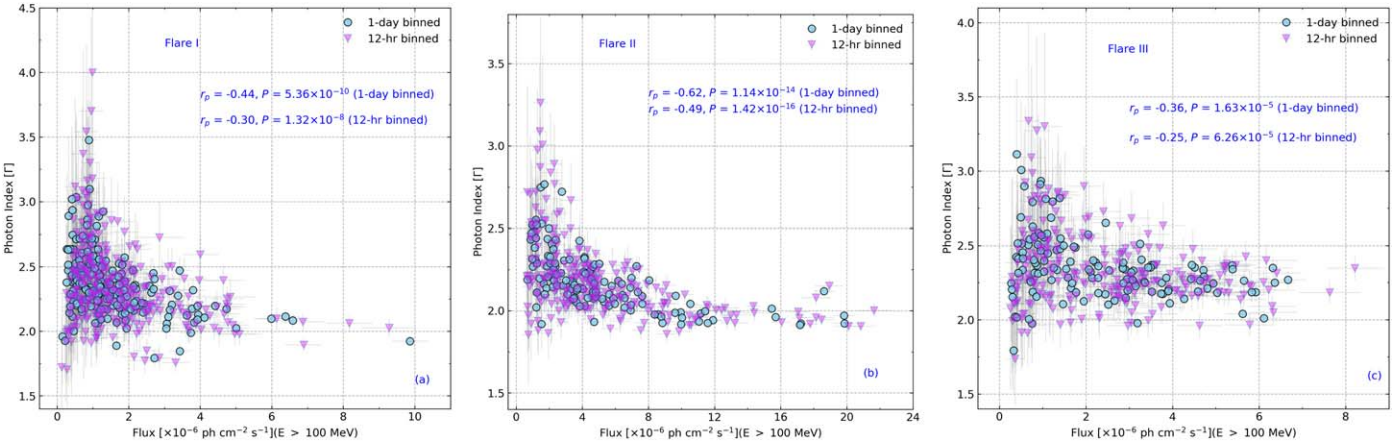

Figure 9. Observed γ-ray photon indices as a function of flux for CTA 102 above 100 MeV. Panels (a), (b), and (c) are the photon indices of the Flare-I, Flare-II, and Flare-III periods, respectively, with 1 day and 12 hr binning. The light cyan points show the 1 day binned data and the light orange points show the 12 hr binned data.

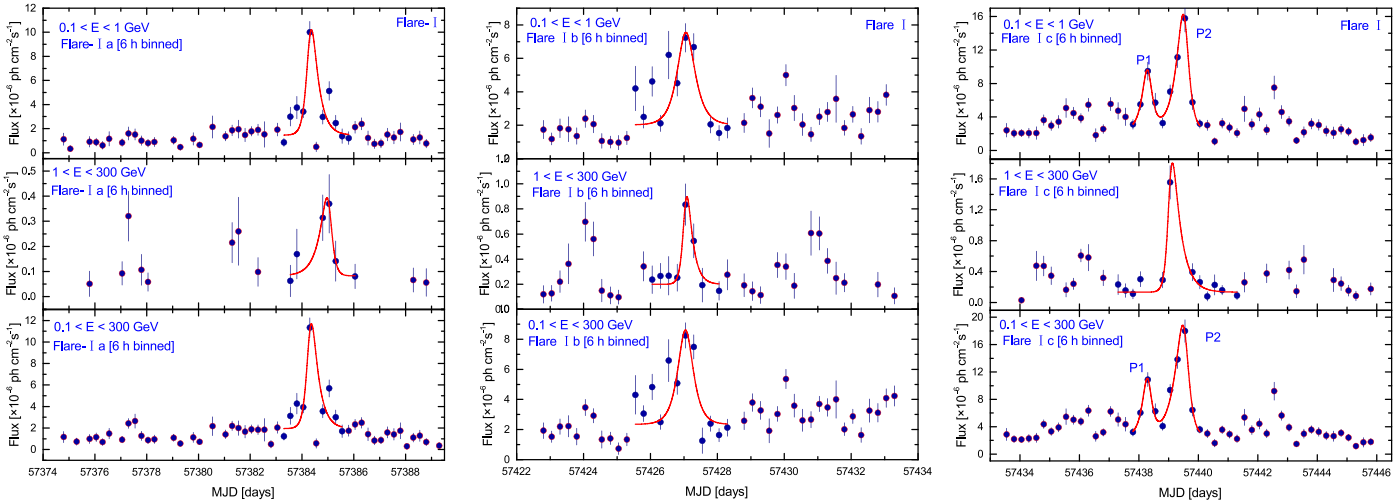

Figure 10. The 6 hr binned light curves of Flare-Ia, Flare-Ib, and Flare-Ic were fitted with Equation (2). Here, we did not consider the data point at MJD 57,438.55, since the decay timescale has a very large error. Points with TS > 9 have been omitted from this figure.

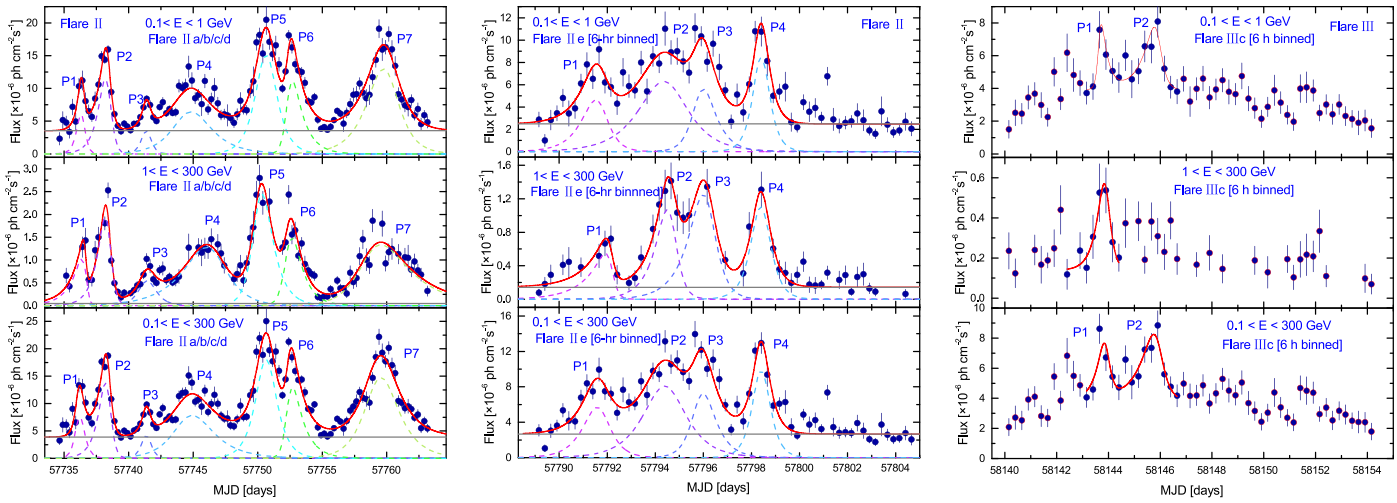

Figure 11. The 6 hr binned light curves of Flare-IIa to Flare-IId, Flare-IIe, and Flare-IIIc were fitted with Equation (2). Points with TS > 9 have been omitted from this figure.

γ-ray photon with energy E when the optical depth of the emitting region is $\tau_{\gamma\gamma} = 1$; m_e is the electron mass; and f_ϵ is the contemporaneous X-ray flux during the γ-ray flare period (Ackermann et al. 2010).

In this work, cutoffs/breaks are actually seen in the spectra. Based on the best-fitting form for the flare period, we adopted a cutoff energy of E_c ($\epsilon = E_c/(m_e c^2)$) to estimate $\delta_{\rm min}$. For a blazar, the bulk Lorentz factor Γ of a radiating blob generally

Table 6
Best-fitting Results of the 6 hr Binned Light Curves of Flares Ia, Ib, and Ic During Flare-I in the Different Energy Bands, as Marked in Figure 10

Energy Band (GeV)	Peak	T_0 (MJD)	F_0 (10^{-6} ph cm^{-2} s^{-1})	T_r (day)	T_f (day)	ξ	T_p (MJD)
			Flare-Ia				
0.1–1		57,384.30	8.21 ± 1.96	0.13 ± 0.04	0.27 ± 0.08	0.35 ± 0.19	57,384.36 ± 0.03
1–300		57,385.05	0.28 ± 0.07	0.32 ± 0.15	0.11 ± 0.05	−0.49 ± 0.25	57,384.96 ± 0.05
0.1–300		57,384.30	9.09 ± 2.15	0.12 ± 0.04	0.26 ± 0.08	0.37 ± 0.20	57,384.36 ± 0.03
			Flare-Ib				
0.1–1		57,427.05	5.52 ± 1.37	0.22 ± 0.11	0.25 ± 0.12	0.06 ± 0.35	57,427.06 ± 0.08
1–300		57,427.05	0.65 ± 0.11	0.08 ± 0.04	0.17 ± 0.04	0.36 ± 0.24	57,427.09 ± 0.02
0.1–300		57,427.05	6.27 ± 1.64	0.20 ± 0.09	0.20 ± 0.09	0.00 ± 0.32	57,427.05 ± 0.06
			Flare-Ic				
0.1–1	P1	57,438.30	6.95 ± 1.30	0.16 ± 0.04	0.13 ± 0.05	−0.10 ± 0.23	57,438.29 ± 0.03
	P2	57,439.55	13.09 ± 1.72	0.25 ± 0.04	0.13 ± 0.03	−0.32 ± 0.13	57,439.49 ± 0.02
1–300	P1	57,439.05	1.44 ± 0.21	0.09 ± 0.02	0.29 ± 0.05	0.53 ± 0.10	57,439.13 ± 0.02
0.1–300	P1	57,438.30	8.02 ± 1.70	0.16 ± 0.05	0.12 ± 0.06	−0.14 ± 0.29	57,438.28 ± 0.04
	P2	57,439.55	15.12 ± 2.26	0.29 ± 0.05	0.13 ± 0.03	−0.38 ± 0.12	57,439.48 ± 0.02

approximates as $\Gamma \sim \delta$; thus, an upper limit on the viewing angle of the jet can be estimated as $\theta_{\rm jet} \sim 1/\delta_{\rm min}$. A lower limit on the Doppler factor of these identified flares (Flare-Ia to Flare-Ic, Flare-IIa to Flare-IIe, and Flare-IIIc) is between 14.6 and 21.0 (see Table 14), which is consistent with the results (a Doppler factor of between 15 and 30) estimated in earlier works (see, e.g., Jorstad et al. 2005; Fromm et al. 2013a, 2013b; Casadio et al. 2015; Jorstad et al. 2017). Recently, Casadio et al. (2019) showed that the Doppler factors of the γ-ray flares during 2016–2017 were $\geqslant$15. They also analyzed the multiwavelength flares of CTA 102 and assumed that such multiwavelength flares could be triggered by interactions between the moving component and the recollimation shock. Viewing angles of 2°.7–3°.9 are obtained here (see Table 14), which are consistent with the results (1°.2 to 3°.9) estimated by Casadio et al. (2015). These results suggest that the jet travels almost directly along the line of sight. However, Raiteri et al. (2017) and D'Ammando et al. (2019) reported a range of viewing angles of 2°–9° in the optical and γ-ray bands, 8°.4–9° at 15 GHz, and 7°–9° at 230 GHz and 37 GHz, respectively. These values suggest that the optical and γ-ray radiation produced by the relativistic jet is characterized by intense wiggling. They assumed that the radio and millimeter-wavelength emitting regions are much more extended along the curved jet than those emitting optical photons. They thus propose that magnetohydrodynamic instabilities or the rotation of the twisted jet may explain the changes in orientation of the different jet regions.

The variability timescale of the source can be used to constrain the size of the emission region. An upper limit on the physical size of the γ-ray emission region can be calculated as:

$$R \leqslant c\, t_{\rm var}\, \delta/(1+z). \tag{6}$$

The sizes of the γ-ray emission regions obtained for the different flux states lie between 0.9×10^{15} cm and 6.0×10^{15} cm, which is close to the result (8.8×10^{15} cm) estimated by Kaur & Baliyan (2018), but less than the result (6.5×10^{16} cm) estimated by Prince et al. (2018).

The upper limit on the angular size (milliarcsec (mas)) of the emission region can be calculated as (Rani et al. 2013b)

$$\varphi \leqslant 0.173\, \frac{(t_{\rm var})/{\rm yr}}{(d_L)/{\rm Gpc}}\, \delta(1+z){\rm mas}, \tag{7}$$

where $t_{\rm var}$ is the variability timescale in years (yr; Marscher et al. 1979) and $d_L = 6.9$ Gpc is the luminosity distance. We found that the angular sizes of the emission region were between 0.1 and 0.2 mas.

5.2. Location of the γ-Ray Emission Region

The distance of the emission region can be constrained by using the observed variability timescale, $d_\gamma \sim 2ct_{\rm var}\Gamma^2/(1+z)$. For blazars, the bulk Lorentz factor, Γ, of a radiating blob generally has $\Gamma \sim \delta_{\rm min}$; thus, we obtained $d_\gamma \sim 0.01$–0.07 pc for the different flaring periods. Considering a conical geometry, the opening angle can be derived as $\theta_{\rm jet} \gtrsim R/d_\gamma$ (Ackermann et al. 2010). The distance of the γ-ray emission region is then estimated using $d_\gamma \sim ct_{\rm var}\delta/\theta_{\rm jet}(1+z)$, where $\theta_{\rm jet} \sim 1/\delta_{\rm min}$; here, we obtained $d_\gamma \sim 0.004$–0.03 pc (see Table 14). It should be noted that this is a crude assumption, as the jet may not have a conical geometry. With this caveat in mind, our results suggest that the γ-ray location of the emission region of the jet may be close to the central black hole.

The energy dependence of the decay timescale of a flare, T_f, can also be used as an alternative approach to constraining the distance of the γ-ray emission region (Dotson et al. 2012). Considering the maximum difference between the decay timescales from the low-energy band $E_{\rm LE}$ (0.1–1 GeV) and the high-energy band $E_{\rm HE}$ (1–300 GeV), $\Delta t_{\rm max} \geqslant T_f$ (LE)–T_f (HE) can be used to estimate an upper limit for the distance of the γ-ray region:

$$d_\gamma < 2.3 \times 10^{18}\Gamma_1[\Delta t_{\rm max,hr}\, L_{\rm MT,45}/(1+z)^{1/2}]^{1/2}, \tag{8}$$

where T_f (LE) and T_f (HE) represent the decay timescales of the flare at low energies (0.1–1 GeV) and high energies (1–300 GeV), respectively; Γ_1 is the bulk Lorentz factor in units of 10, where $\Gamma_1 \sim \delta_{\rm min}/10$; and $L_{\rm MT,45}$ is the molecular torus (MT) luminosity in units of 10^{45} erg s^{-1}, which is

Table 7
Best-fitting Results of the 6 hr Binned Light Curves of Flare-IIa to Flare-IId and Flare-IIe During Flare-II in the Different Energy Bands, as Marked in Figure 11

Peak	T_0 (MJD)	F_0 (10^{-6} ph cm^{-2} s^{-1})	T_r (day)	T_f (day)	ξ	T_p (MJD)
			Flare-IIa/b/c/d (0.1–1 GeV)			
P1	57,736.41	7.00 ± 2.18	0.31 ± 0.13	0.17 ± 0.09	−0.29 ± 0.31	57,736.34 ± 0.07
P2	57,738.41	11.31 ± 0.80	0.62 ± 0.08	0.23 ± 0.03	−0.46 ± 0.07	57,738.24 ± 0.03
P3	57,741.41	4.00 ± 0.72	0.32 ± 0.10	0.27 ± 0.10	−0.08 ± 0.24	57,741.39 ± 0.07
P4	57,744.66	6.43 ± 0.76	1.17 ± 0.21	1.55 ± 0.31	0.14 ± 0.13	57,744.85 ± 0.18
P5	57,750.66	15.51 ± 1.36	0.73 ± 0.09	0.73 ± 0.15	0.00 ± 0.12	57,750.66 ± 0.09
P6	57,752.41	9.81 ± 1.36	0.23 ± 0.07	0.90 ± 0.10	0.59 ± 0.11	57,752.66 ± 0.03
P7	57,759.91	13.00 ± 0.93	1.26 ± 0.13	0.94 ± 0.11	−0.15 ± 0.08	57,759.75 ± 0.08
			Flare-IIa/b/c/d (1–300 GeV)			
P1	57,736.66	0.80 ± 0.26	0.96 ± 0.38	0.10 ± 0.09	−0.81 ± 0.17	57,736.46 ± 0.10
P2	57,738.41	1.87 ± 0.17	0.67 ± 0.11	0.23 ± 0.04	−0.49 ± 0.09	57,738.23 ± 0.04
P3	57,741.41	0.57 ± 0.11	0.55 ± 0.20	0.61 ± 0.24	0.05 ± 0.27	57,741.44 ± 0.16
P4	57,746.41	1.25 ± 0.16	1.91 ± 0.36	1.16 ± 0.31	−0.24 ± 0.15	57,746.05 ± 0.21
P5	57,750.16	2.45 ± 0.27	0.51 ± 0.10	0.86 ± 0.30	0.26 ± 0.19	57,750.33 ± 0.14
P6	57,752.41	1.40 ± 0.32	0.32 ± 0.14	0.86 ± 0.14	0.46 ± 0.18	57,752.64 ± 0.06
P7	57,758.91	1.24 ± 0.15	1.11 ± 0.18	2.54 ± 0.42	0.39 ± 0.10	57,759.55 ± 0.17
			Flare-IIa/b/c/d (0.1–300 GeV)			
P1	57,736.16	8.62 ± 2.13	0.24 ± 0.10	0.33 ± 0.13	0.16 ± 0.30	57,736.20 ± 0.08
P2	57,738.41	13.51 ± 0.10	0.61 ± 0.09	0.22 ± 0.03	−0.47 ± 0.08	57,738.25 ± 0.03
P3	57,741.41	4.76 ± 0.90	0.32 ± 0.10	0.27 ± 0.10	−0.08 ± 0.24	57,741.39 ± 0.07
P4	57,744.66	7.74 ± 0.87	1.14 ± 0.20	1.70 ± 0.32	0.20 ± 0.12	57,744.93 ± 0.17
P5	57,750.66	18.59 ± 1.59	0.71 ± 0.09	0.71 ± 0.14	0.00 ± 0.12	57,750.66 ± 0.08
P6	57,752.41	11.40 ± 1.52	0.23 ± 0.07	0.92 ± 0.10	0.60 ± 0.10	57,752.67 ± 0.03
P7	57,759.41	14.76 ± 1.05	1.03 ± 0.11	1.32 ± 0.13	0.12 ± 0.07	57,759.55 ± 0.08
			Flare-IIe (0.1–1 GeV)			
P1	57,791.66	4.54 ± 1.11	0.63 ± 0.19	0.36 ± 0.18	−0.27 ± 0.27	57,791.53 ± 0.11
P2	57,794.41	6.31 ± 1.13	0.97 ± 0.29	0.86 ± 0.86	−0.06 ± 0.52	57,794.36 ± 0.45
P3	57,795.91	5.59 ± 3.74	0.33 ± 0.35	0.52 ± 0.23	0.22 ± 0.55	57,796.00 ± 0.19
P4	57,798.41	8.82 ± 1.57	0.30 ± 0.07	0.30 ± 0.06	0.00 ± 0.15	57,798.41 ± 0.05
			Flare-IIe (1–300 GeV)			
P1	57,792.16	0.42 ± 0.10	0.85 ± 0.28	0.13 ± 0.08	−0.70 ± 0.16	57,791.95 ± 0.06
P2	57,794.66	1.02 ± 0.29	0.56 ± 0.11	0.24 ± 0.16	−0.40 ± 0.29	57,794.52 ± 0.06
P3	57,796.16	1.21 ± 0.23	0.67 ± 0.32	0.35 ± 0.09	−0.31 ± 0.24	57,796.01 ± 0.14
P4	57,798.41	1.14 ± 0.22	0.37 ± 0.09	0.34 ± 0.06	−0.04 ± 0.15	57,798.40 ± 0.05
			Flare-IIe (0.1–300 GeV)			
P1	57,791.66	5.72 ± 1.15	0.58 ± 0.16	0.43 ± 0.18	−0.15 ± 0.25	57,791.59 ± 0.12
P2	57,794.41	8.13 ± 1.29	0.81 ± 0.22	0.78 ± 0.69	−0.02 ± 0.46	57,794.40 ± 0.36
P3	57,795.91	7.26 ± 3.97	0.35 ± 0.32	0.52 ± 0.17	0.20 ± 0.47	57,795.99 ± 0.17
P4	57,798.41	10.23 ± 1.60	0.32 ± 0.07	0.32 ± 0.06	0.00 ± 0.14	57,798.41 ± 0.05

$L_{\rm MT,45} = 7.0$ for CTA 102 (Malmrose et al. 2011). Here, if the flares include some substructure, the maximum decay time difference can be found by comparing against the decay timescales of each substructure within the 0.1–1 GeV and 1–300 GeV bands. The modeling parameters are described in Tables 6–9. We obtained an upper limit for the distance of the γ-ray emission region from the central engine of $d_\gamma < 17.4$ pc (see Table 14, column 17).

Our analysis suggests that the locations of the γ-ray emission arising from the flares are smaller than 17.4 pc, which is consistent with the result of $d_\gamma < 16.7$ pc estimated by Li et al. (2018). The derived distance of the γ-ray emitting region is less than the radio core distances $r_{\rm core,43GHz} = 46.7$ pc (Pushkarev et al. 2012), $r_{\rm core,43GHz} = 22.9$ pc (Li et al. 2018), and $r_{\rm core,8.6GHz} = 83.8$ pc (Algaba et al. 2017), implying that the location of the γ-ray emission region of CTA 102 may lie in the inner jet upstream of the radio core (Li et al. 2018).

The mechanism(s) for producing the γ-ray emission is still a matter of debate, and, according to one approach, is thought to arise from inverse Compton (IC) scattering of low-energy seed photons by highly energetic leptons in the jets. At a few pc from the supermassive black hole (SMBH), the seed photons as EC radiation are dominated by infrared radiation. In this region, the electrons during the major flaring activity can be accelerated to higher energies by magnetic reconnection. During the nonflaring activity, the acceleration from magnetic reconnection is not very effective, so the electrons may be accelerated to higher energies by the shocks arising from the

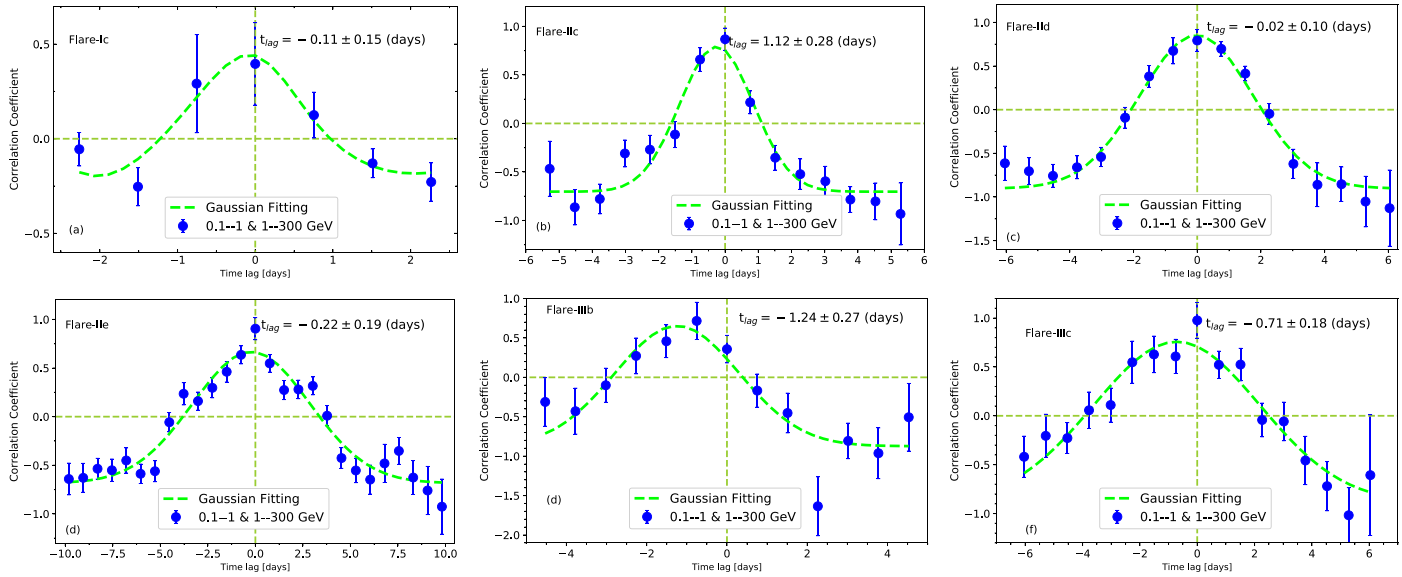

Figure 12. DCF calculated for the 6 hr binned light curves in the 0.1–1 GeV and 1–300 GeV energy bands. The Flare-Ia to Flare-Ib, Flare-IIa to Flare-IIb, and Flare-IIIa periods were not considered due to poor data statistics.

Table 8
Best-fitting Results of the 6 hr Binned Light Curves of Flare-IIIc During Flare-III in the Different Energy Bands, as Marked in Figure 11

Peak	T_0 (MJD)	F_0 (10^{-6} ph cm^{-2} s^{-1})	T_r (day)	T_f (day)	ξ	T_p (MJD)
			Flare-IIIc (0.1–1 GeV)			
P1	58,143.66	3.32 ± 0.87	0.07 ± 0.07	0.25 ± 0.08	0.56 ± 0.36	58,143.73 ± 0.02
P2	58,145.91	3.39 ± 0.65	0.48 ± 0.13	0.17 ± 0.06	−0.48 ± 0.17	58,145.78 ± 0.04
			Flare-IIIc (1–300 GeV)			
	58,143.91	0.41 ± 0.07	0.30 ± 0.08	0.16 ± 0.05	−0.30 ± 0.19	58,143.84 ± 0.04
			Flare-IIIc (0.1–300 GeV)			
P1	58,143.91	3.35 ± 1.15	0.30 ± 0.16	0.16 ± 0.09	−0.30 ± 0.35	58,143.84 ± 0.08
P2	58,145.91	3.93 ± 1.16	0.58 ± 0.24	0.22 ± 0.13	−0.45 ± 0.29	58,145.76 ± 0.09

Table 9
Values of the Constant Flux and χ^2/ndf from the Fitted Profiles in Figures 10 and 11

Flare	Constant Flux ($\times 10^{-6}$ ph cm^{-2} s^{-1})			χ^2/ndf		
	0.1–1 GeV	1–300 GeV	0.1–300 GeV	0.1–1 GeV	1–300 GeV	0.1–300 GeV
			Flare-I			
Flare-Ia	1.46 ± 0.52	0.08 ± 0.02	1.95 ± 0.65	27.80/6 = 4.63	0.77/2 = 0.38	26.69/5 = 5.34
Flare-Ib	2.02 ± 0.59	0.20 ± 0.03	2.34 ± 0.54	21.66/7 = 3.09	1.74/4 = 0.43	32.91/8 = 4.11
Flare-Ic	2.45 ± 0.72	0.13 ± 0.03	2.57 ± 1.00	3.90/3 = 1.30	7.39/8 = 0.92	7.01/3 = 2.34
			Flare-II			
Flare-IIa/b/c/d	3.54 ± 0.39	0.05 ± 0.11	3.88 ± 0.44	275.81/93 = 2.97	152.22/70 = 2.17	369.87/93 = 4.00
Flare-IIe	2.48 ± 0.21	0.14 ± 0.02	2.67 ± 0.23	119.89/50 = 2.40	35.85/30 = 1.19	146.98/50 = 2.94
			Flare-III			
Flare-IIIc	3.90 ± 0.40	0.14 ± 0.04	3.87 ± 1.04	4.72/8 = 0.59	1.59/4 = 0.40	11.72/8 = 1.47

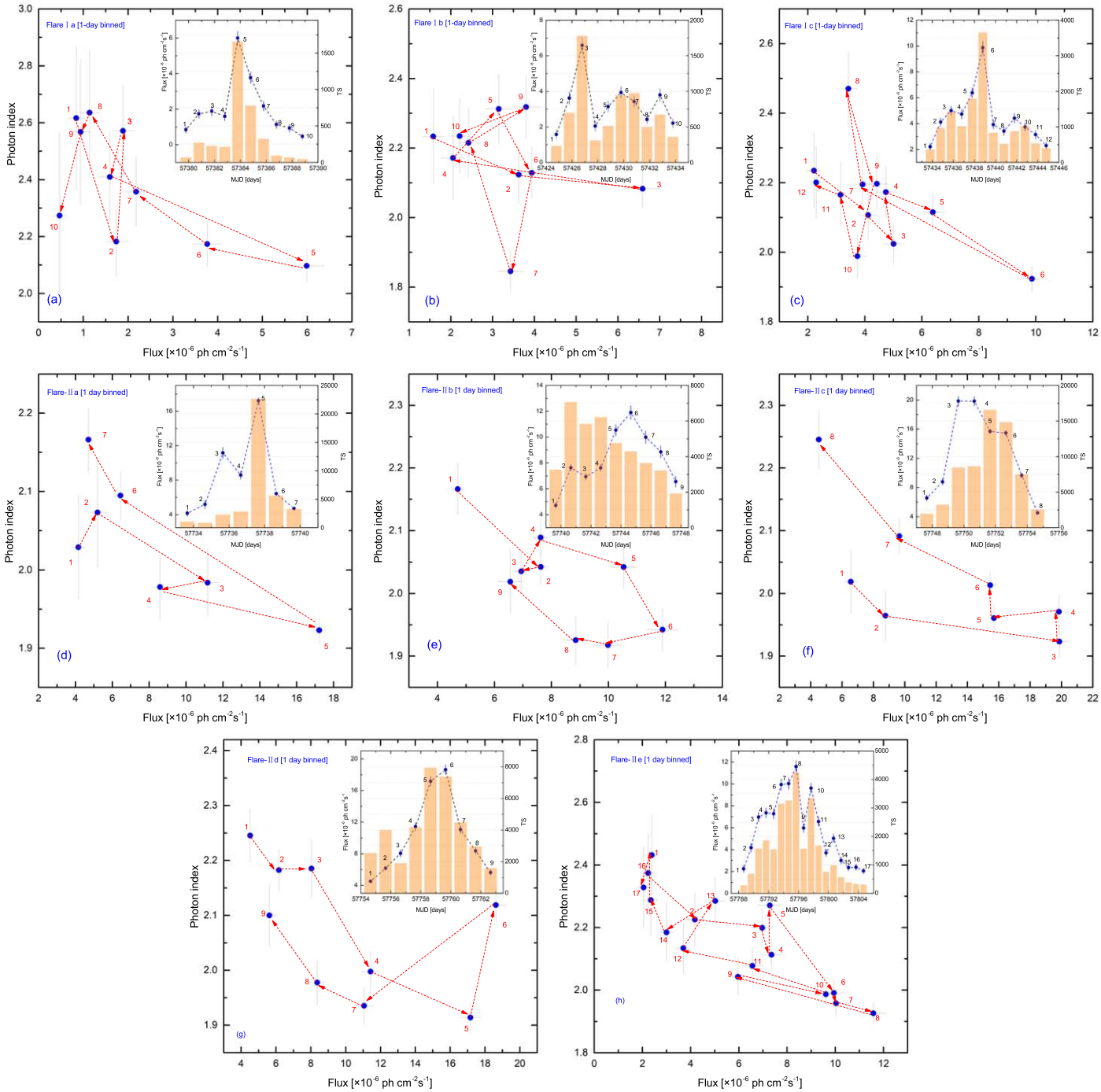

Figure 13. Variation of the photon indices as a function of the observed fluxes of the flares, using 1 day binned data. Panels (a)–(c) present Flare-Ia to Flare-Ic during the Flare-I period. Panels (d)–(h) present Flare-IIa to Flare-IIe during the Flare-II period.

interaction of the jet with the external medium, scattering the low-energy seed photons.

5.3. γ-Ray Variability of CTA 102

The source exhibited three γ-ray outbursts (Flare-I, Flare-II, and Flare-III) with average photon indices of 2.30, 2.16, and 2.34, respectively. Their peak fluxes are larger than 5.20×10^{-6} ph cm^{-2}s^{-1}, and are 25 times larger than during the low state (0.19×10^{-6} ph cm^{-2}s^{-1}). The 1 day and 12 hr binned flux distributions of Flare-I are consistent with a log-normal distribution, while the 1 day and 12 hr binned flux distributions of Flare-II and Flare-III show a double log-normal behavior, which has also been found for other bright blazars (see, e.g., Kushwaha et al. 2016; Shah et al. 2018; Sinha et al. 2018; Ait Benkhali et al. 2019; Khatoon et al. 2020). These results seem to support the notion that the γ-ray emission regions of CTA 102 vary from one flare to another, which is consistent with the results of Prince et al. (2017). Sinha et al. (2018) showed that the non-Gaussian flux distributions observed for blazars may be associated with linear Gaussian variations of intrinsic particle acceleration or escape timescales. The log-normal distributions of the observed flux may suggest multiplicative perturbations associated with the emission

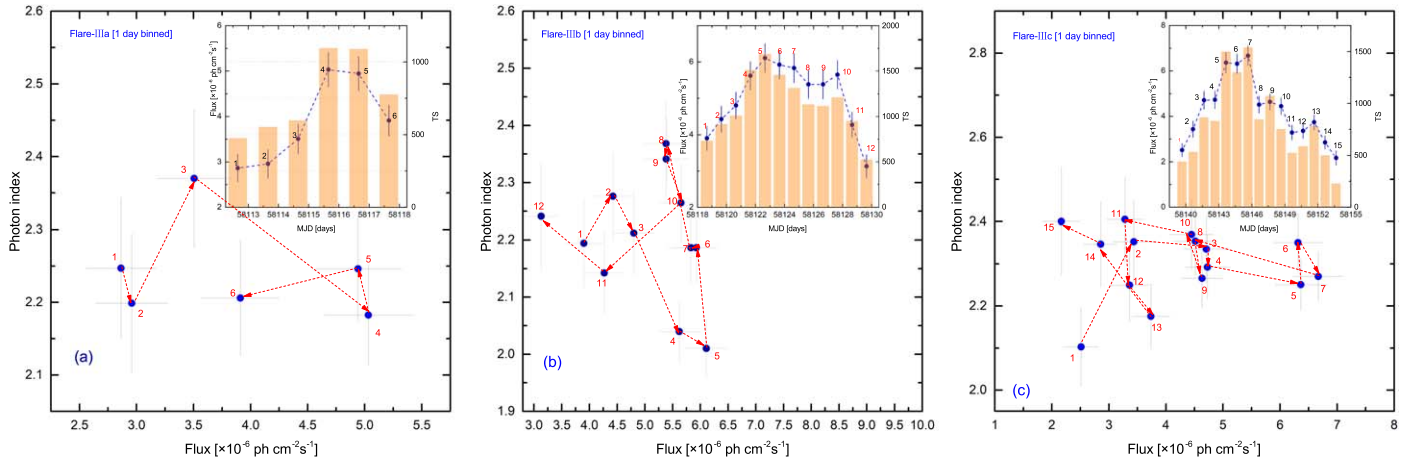

Figure 14. Variation of the photon indices as a function of the observed fluxes of the flares using 1 day binned data. Panels (a), (b), and (c) present the relations of Flare-IIIa, Flare-IIIb, and Flare-IIIc during the Flare-III period.

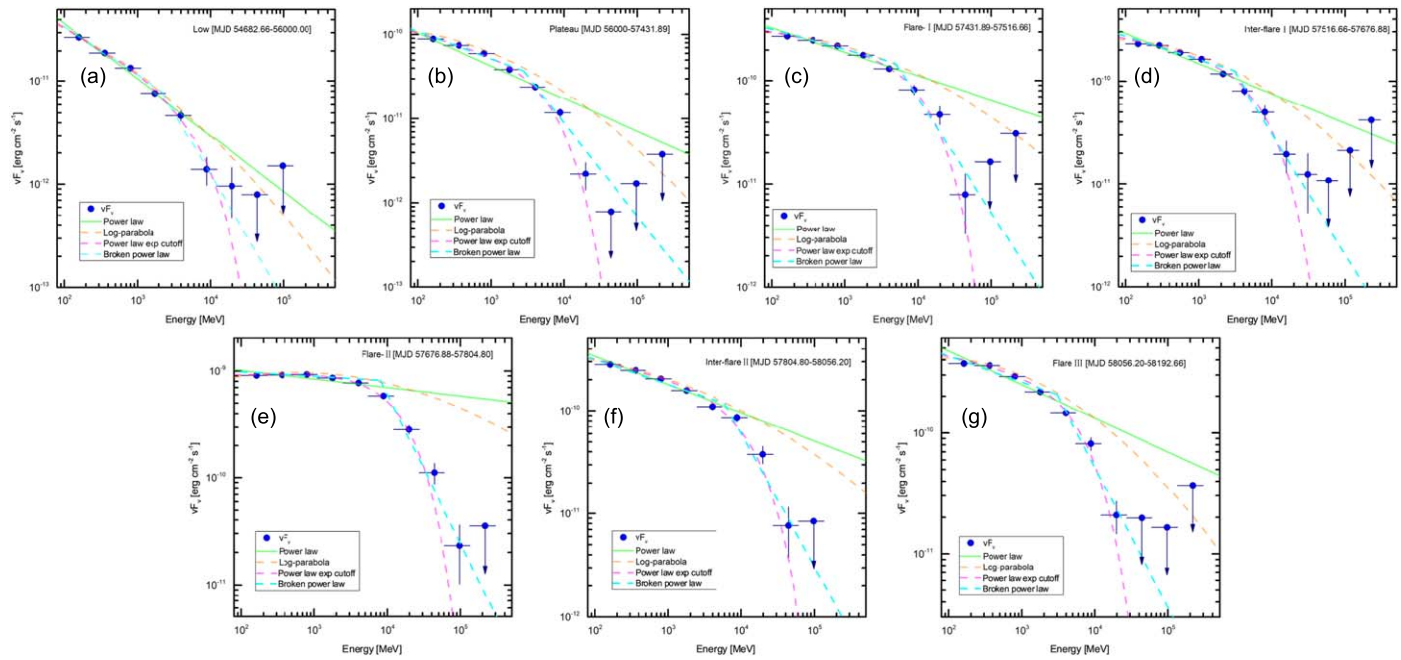

Figure 15. γ-ray SEDs of CTA 102 during the different states defined in Figure 1. These states were fitted by PL (green lines), LP (orange dashed curves), PLEC (magenta dashed curves), and BPL (cyan dashed curves) spectral models. Their respective best-fitting parameters are given in Table 10.

process(es) (see, e.g., Lyubarskii 1997; Arévalo & Uttley 2006; Shah et al. 2018). These processes, including particle acceleration and diffusion, can modify the shape of the emitted electron distributions, which may account for the various flux distributions found here. For CTA 102, we find that the flux distributions of Flare-II and Flare-III show a double log-normal behavior. The statistics of the 1 day and 12 hr binned index distributions from Flare-I, Flare-II, and Flare-III are not statistically significant. Hence, these results should only be taken as tentative indicators of the underlying emission mechanism(s).

Another feature of the light curves involves the temporal profiles of the peaks. In our study, we find that five of the peaks seen in the 3 hr binned light curves have $T_r > T_d$ ($\xi < -0.3$), five of the peaks have $T_r < T_d$ ($\xi > 0.3$), and 14 of the peaks have $T_r \sim T_d$ ($-0.3 \leqslant \xi \leqslant 0.3$; see Table 2 and Figure 20(a)). For the 6 hr binned light curves, 12 of the peaks have $T_r > T_d$, 9 of the peaks have $T_r < T_d$, and 28 of the peaks have $T_r \sim T_d$ (see Tables 6–8 and Figure 20(b)). We find that the majority of peaks in the 3 hr and 6 hr binned light curves have a symmetric temporal profile within the error bars.

The detection of symmetric/asymmetric flares is related to some of the specific characteristics of the flares (e.g., spectral properties, flux levels, acceleration, cooling timescales, etc.). A symmetric flare can be seen if the cooling time of the emitting particles is much smaller than the time interval from the interaction of the shock wave with the jet plasma (Blandford & Königl 1979; Chatterjee et al. 2012). In the case of a disturbance in the jet moving through a standing shock, the rise/decay time corresponds to the time taken by the disturbance to enter/leave the standing shock region. In this case, the rise and decay times will be similar, resulting in a symmetric flare (Chatterjee et al. 2012). For the source CTA 102, the symmetric temporal profiles observed for the flares suggest that the rise and decay timescales are dominated by the crossing time of the radiation or a disturbance from a

Table 10
Fermi-LAT SEDs of the Different Activity States from the 7 Day Binned Light Curves, as Defined in Figure 1(a)

PL						
Activity	Γ					
Low	2.54 ± 0.02				⋯	⋯
Plateau	2.39 ± 0.01				⋯	⋯
Flare-I	2.23 ± 0.01				⋯	⋯
Interflare-I	2.29 ± 0.01				⋯	⋯
Flare-II	2.08 ± 0.01				⋯	⋯
Interflare-II	2.27 ± 0.01				⋯	⋯
Flare-III	2.28 ± 0.01				⋯	⋯
LP						
Activity	α	β			TS_{curve}	Curvature Significance
Low	2.44 ± 0.03	0.08 ± 0.02			27.18	4.5σ
Plateau	2.24 ± 0.02	0.11 ± 0.01			271.18	$>5\sigma$
Flare-I	2.13 ± 0.02	0.07 ± 0.01			96.24	$>5\sigma$
Interflare-I	2.15 ± 0.02	0.10 ± 0.01			114.38	$>5\sigma$
Flare-II	1.97 ± 0.01	0.06 ± 0.01			424.58	$>5\sigma$
Interflare-II	2.18 ± 0.01	0.06 ± 0.01			114.04	$>5\sigma$
Flare-III	2.14 ± 0.02	0.11 ± 0.01			196.02	$>5\sigma$
PLEC						
Activity	Γ			E_c (GeV)	TS_{curve}	Curvature Significance
Low	2.42 ± 0.03			7.44 ± 1.84	30.62	4.9σ
Plateau	2.22 ± 0.01			5.84 ± 0.51	254.50	$>5\sigma$
Flare-I	2.13 ± 0.01			12.46 ± 1.60	103.64	$>5\sigma$
Interflare-I	2.14 ± 0.02			7.11 ± 0.92	107.54	$>5\sigma$
Flare-II	1.98 ± 0.01			14.86 ± 0.93	501.54	$>5\sigma$
Interflare-II	2.18 ± 0.01			13.00 ± 1.59	118.44	$>5\sigma$
Flare-III	2.13 ± 0.02			6.70 ± 0.72	173.92	$>5\sigma$
BPL						
Activity	Γ_1	Γ_2	$\Delta\Gamma$	E_{break} (GeV)	TS_{curve}	Curvature Significance
Low	2.48 ± 0.05	3.21 ± 0.13	0.73 ± 0.14	2.21 ± 0.16	28.64	4.7σ
Plateau	2.32 ± 0.01	3.31 ± 0.09	0.99 ± 0.09	2.78 ± 0.11	205.46	$>5\sigma$
Flare-I	2.19 ± 0.01	3.11 ± 0.13	0.92 ± 0.13	4.90 ± 0.27	84.34	$>5\sigma$
Interflare-I	2.22 ± 0.01	3.17 ± 0.12	0.95 ± 0.12	3.00 ± 0.06	90.50	$>5\sigma$
Flare-II	2.04 ± 0.01	3.40 ± 0.14	1.35 ± 0.14	8.00 ± 0.59	435.40	$>5\sigma$
Interflare-II	2.24 ± 0.01	3.29 ± 0.15	1.05 ± 0.15	6.03 ± 0.27	91.88	$>5\sigma$
Flare-III	2.21 ± 0.01	3.16 ± 0.16	0.94 ± 0.16	3.04 ± 0.44	133.56	$>5\sigma$

Note. Column (1): the different states of the 7 day binned light curves; columns (2)–(3): spectral indices and curvature indices from the different models, respectively; column (4): spectral slopes ($\Delta\Gamma = \Gamma_2$-Γ_2) from the BPL model; column (5): break energies (E_c and E_{break}) from the PLEC and BPL models, respectively; columns (6)–(7): the significance estimated by two times the difference between the log(likelihood) values for the two spectral models, which is distributed as χ^2 with Δn degrees of freedom. The parameter Δlog(likelihood) is the difference between the $-$log(likelihood) value of the LP, PLEC, and BPL models with respect to the PL model, and -2Δlog(likelihood) $= TS_{curve}$ was used to evaluate the significances of the spectral curvatures.

dense plasma blob passing through the standing shock front in the jet region.

For a flare in which the acceleration timescales are much less than the cooling timescale, the particles are rapidly accelerated to higher energies, so that after approximately one acceleration, the acceleration region has moved all the particles up to their maximum energies. At subsequent times, the particles slowly cool. In this case, the rise and decay times are not similar, resulting in an asymmetric temporal profile (Kirk & Mastichiadis 1999). In this work, an asymmetric temporal profile would be expected to arise from the fast injection of accelerated particles or an escape from the emission region (see, e.g., Sikora et al. 2001; Joshi & Böttcher 2011; Rani et al. 2013b; Joshi et al. 2014; Roy et al. 2019).

5.4. Origin of the Extreme γ-Ray Flares of CTA 102

Our results show a series of substructures within the outbursts. To determine the duration of the shortest flux variability, we scanned all of the 3 hr binned light curves by

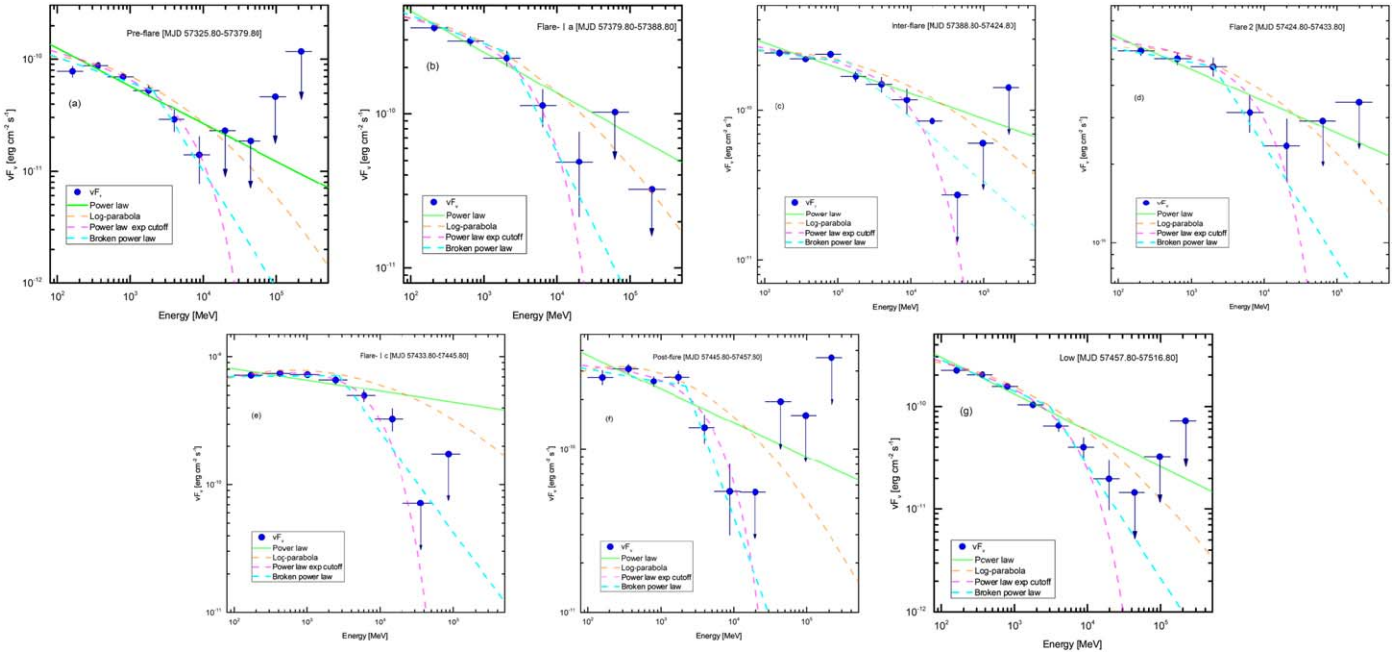

Figure 16. γ-ray spectra of CTA 102 during the different states of Flare-I defined in Figure 2. These states were fitted by PL (green curve), LP (orange curve), BPL (cyan curve), and PLEC (magenta curve) spectral models. Their respective best-fitting parameters are given in Table 11.

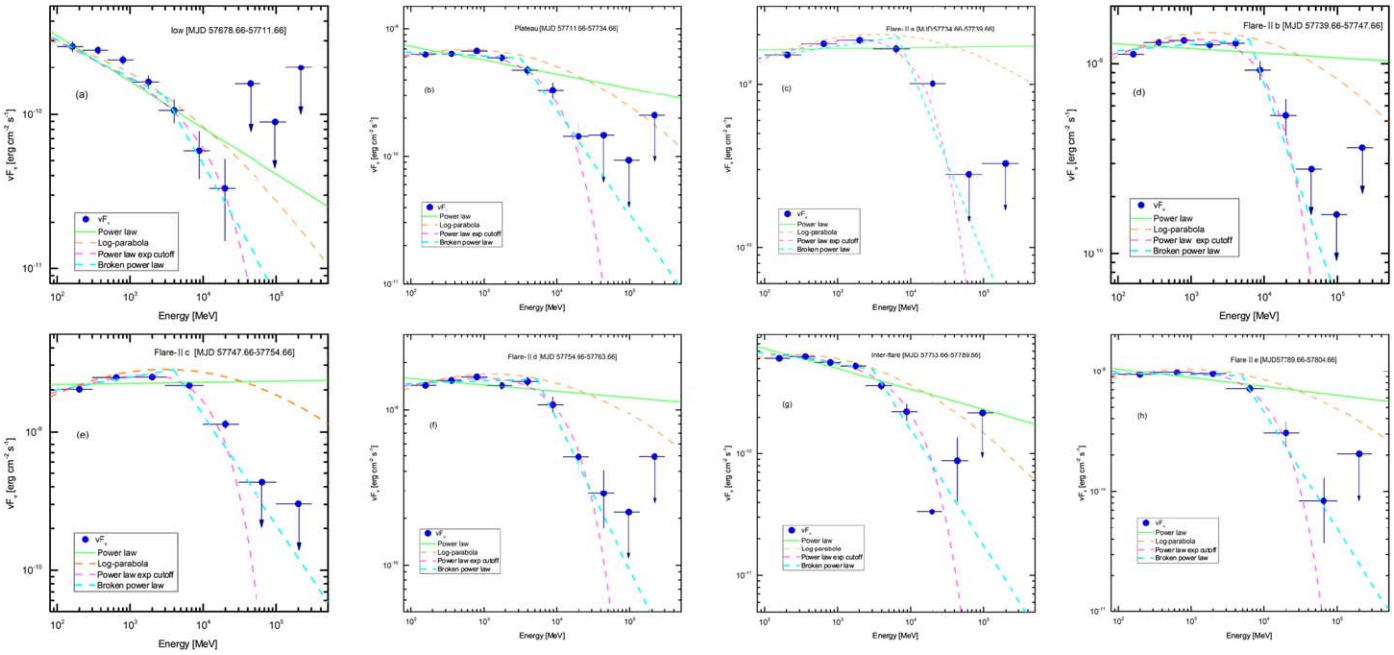

Figure 17. γ-ray spectra of CTA 102 during the different states of Flare-II defined in Figure 4. These states were fitted by PL (green curve), LP (orange curve), BPL (cyan curve), and PLEC (magenta curve) spectral models. Their respective best-fitting parameters are given in Table 12.

comparing consecutive light-curve points with the following equation:

$$F(t_2) = F(t_1)2^{(\tau^{-1}(t_2-t_1))}, \quad (9)$$

where τ is the doubling/halving timescale and $F(t_2)$ and $F(t_1)$ are the fluxes at times t_2 and t_1, respectively. In this work, it is worth pointing out that when scanning the 3 hr binned light curves, two conditions had to be satisfied: (1) the flux was doubled/halved between two successive instants of time; and (2) the TS values of these two consecutive time instants were $\geqslant 25$ ($\sim 5\sigma$ detection; see, e.g., Prince et al. 2017, 2018; Das et al. 2020).

The scanning results are provided in Table 15. The rise and decay timescales are distributed around means of 1.10 ± 0.03 hr and 1.11 ± 0.04 hr (see Figure 21), respectively. The fastest rise timescale is 0.70 ± 0.05 hr, during MJD 57,384.17–57,384.30, and the shortest is 0.79 ± 0.27 hr, during MJD 57,792.41–57,792.53 (see Figure 21). Such γ-ray flares with similar timescales have also been observed for other bright Fermi blazars, such as PKS B1222+216, S5 0836+71, 3C 279, 3C 454.3, PKS 1510-089, and PKS 1502+106 (see, e.g.,

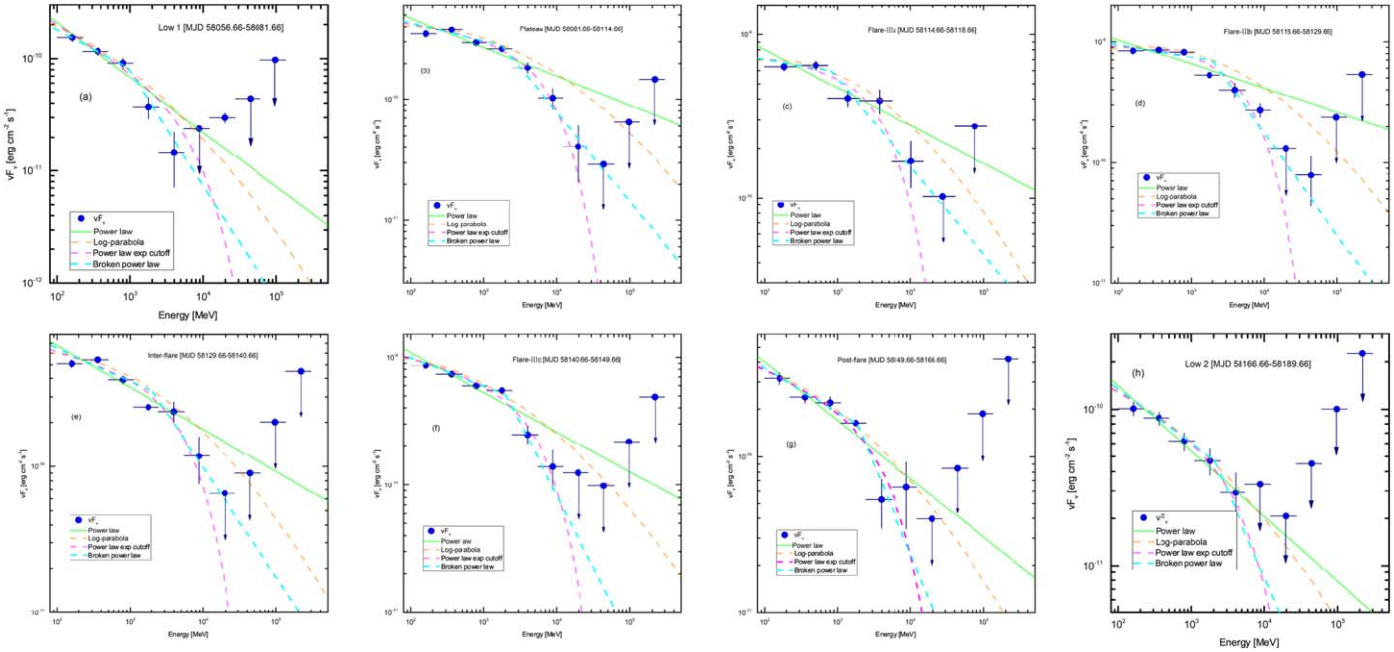

Figure 18. γ-ray spectra of CTA 102 during the different states of Flare-III defined in Figure 7. These states were fitted by PL (green curve), LP (orange curve), BPL (cyan curve), and PLEC (magenta curve) spectral models. Their respective best-fitting parameters are given in Table 13.

Foschini et al. 2011; Paliya 2015a; Ackermann et al. 2016; Britto et al. 2016; Prince et al. 2017; Ding et al. 2019; Orienti et al. 2020).

Aharonian et al. (2017) proposed three scenarios to explain the ultrafast γ-ray variability in AGNs: (1) a magnetospheric model, which is usually applied to non-blazar-type AGNs, as their γ-ray luminosities are quite modest compared to those of blazars; (2) magnetic reconnection, which is usually triggered by the shock compression of magnetic fields in a plasma (see, e.g., Komissarov 2003; Lyubarsky 2005); and (3) the interaction of a jet with some external obstacle, e.g., a broad-line region (BLR) cloud or a star.

If magnetic reconnection is realized in AGN jets, it can result in ultrafast γ-ray flares in blazar-type AGNs with variability timescales significantly shorter than r_g/c (Giannios et al. 2009), where $r_g = 1.5 \times 10^{14} M_9$ cm is the gravitational radius, which, for CTA 102, is $r_g \sim 1.3 \times 10^{14}$ cm. Thus, we obtain $r_g/c = 1.20$ hr. This value is slightly larger than the CTA 102 rise timescale of 1.10 hr (average value) and decay timescale of 1.11 hr (see Figure 21 and Table 15).

Three-dimensional numerical simulations have shown that ultrafast γ-ray flares may be triggered by magnetic reconnection, which could further drive strong stochastic acceleration and form a hard electronic energy spectrum with an electronic spectral index of $\sim$1 (a spectral index $p < 2$ is usually considered to be a hard spectrum; Guo et al. 2014, 2015). Prince et al. (2017) modeled the SEDs of four flares (flare 1 during MJD 57,735–57,740, flare 2 during MJD 57,740–57,748, flare 3 during MJD 57,748–57,756, and flare 4 during MJD 57,756–57,763) with multiwavelength data, and they found that the spectral index of the injected electron spectrum was $\sim$1.7 (see Figures 7 and 8 and Table 5 of Prince et al. 2017), which implies a hard spectrum for CTA 102. Morris et al. (2019) found that by fitting SEDs from the 2016 TeV flare of BL Lacertae with simultaneous multiwavelength data, magnetic reconnection may be able to produce the rapid, powerful TeV flares. Recently, Shukla & Mannheim (2020) have shown that if the γ-ray flare was caused by magnetic reconnection, this implies that the distance of the γ-ray emission region is approximately a few pc from the center of the SMBH. In these regions, magnetic reconnections are triggered by instabilities disrupting the collimated jet flow, so the reconnection layer fragments into small plasmoids that interact with each other and grow into monster plasmoids within the reconnection region. These massive plasmoids lead to the formation of minijets, which produce optically thin rapid γ-ray flares (Giannios et al. 2009; Shukla & Mannheim 2020). Based on this scenario, we suggest that the γ-ray emission region in CTA 102 is located a few pc from the SMBH, and that the extreme γ-ray flare of CTA 102 is likely to be caused by magnetic reconnection.

Araudo et al. (2010) have shown that the jets interacting with BLR clouds can result in the formation of strong shocks, in which NT particles can be accelerated through diffusive shock acceleration. When BLR clouds penetrate into a jet with a short timescale, the impact on the relativistic jet from the surface of the cloud can lead to the formation of two shocks: a shock propagating in the cloud and a bow-shock propagating in the jet material (Araudo et al. 2009, 2010; del Palacio et al. 2019). If the clouds fully penetrate into the jet, the BLR cloud velocity ($\vartheta_{c,0}$) outside the jet will be larger than the shock velocity ($\vartheta_{\rm sh}$). If this condition is not fulfilled, the cloud can be destroyed by the jet's ram pressure. Thus, a minimum interaction height $z_{\rm min}$ (cm) is obtained to avoid cloud disruption before full penetration:

$$z_{\rm min} = \frac{1}{\vartheta_{c,0}\,\theta_{\rm jet}}\sqrt{\frac{L_j}{\pi c m_p n_{c,0}}} \approx 5 \times 10^{15}\left(\frac{0.1}{\theta_{\rm jet}}\right)\left(\frac{10^9}{\vartheta_{c,0}}\right)\sqrt{\left(\frac{10^{10}}{n_{c,0}}\right)\left(\frac{L_j}{10^{44}}\right)}\ {\rm cm}, \quad (10)$$

where $\vartheta_{c,0} \approx \sqrt{\frac{GM}{R_{\rm BLR}}} \approx 0.43 \times 10^9$ cm s^{-1} is the BLR cloud velocity, m_p (g) is the mass of the proton (Araudo et al. 2009),

Table 11
Fermi-LAT SEDs During the Different States of Flare-I, as Defined in Figure 2

PL						
Activity	Γ					
Preflare	2.34 ± 0.04				⋯	⋯
Flare-Ia	2.26 ± 0.04				⋯	⋯
Interflare	2.17 ± 0.02				⋯	⋯
Flare-Ib	2.12 ± 0.03				⋯	⋯
Flare-Ic	2.09 ± 0.02				⋯	⋯
Postflare	2.21 ± 0.03				⋯	⋯
Low	2.35 ± 0.02				⋯	⋯
LP						
Activity	Luminosity (10^{48} erg s^{-1})	α	β		TS_{curve}	Curvature Significance
Preflare	2.17 ± 0.06	0.12 ± 0.03			18.00	3.8σ
Flare-Ia	2.16 ± 0.05	0.08 ± 0.03			8.20	1.7σ
Interflare	2.06 ± 0.04	0.06 ± 0.02			16.80	3.4σ
Flare-Ib	2.03 ± 0.04	0.05 ± 0.02			8.00	2.0σ
Flare-Ic	1.95 ± 0.02	0.08 ± 0.01			33.20	4.9σ
Postflare	2.02 ± 0.05	0.12 ± 0.02			23.80	4.2σ
Low	2.23 ± 0.03	0.11 ± 0.02			44.20	$>5\sigma$
PLEC						
Activity	Γ			E_c (GeV)	TS_{curve}	Curvature Significance
Preflare	2.19 ± 0.06			7.11 ± 2.58	12.20	3.7σ
Flare-Ia	2.12 ± 0.06			7.03 ± 2.93	11.20	2.3σ
Interflare	2.08 ± 0.03			16.85 ± 5.52	19.00	3.7σ
Flare-Ib	2.05 ± 0.04			20.78 ± 8.50	9.80	2.3σ
Flare-Ic	1.94 ± 0.03			9.19 ± 1.91	45.40	$>5\sigma$
Postflare	2.03 ± 0.06			6.56 ± 2.27	19.40	3.7σ
Low	2.21 ± 0.03			7.00 ± 1.60	36.00	$>5\sigma$
BPL						
Activity	Γ_1	Γ_2	$\Delta\Gamma$	E_{break} (GeV)	TS_{curve}	Curvature Significance
Preflare	2.24 ± 0.04	3.04 ± 0.28	0.80 ± 0.28	2.03 ± 0.39	13.60	3.3σ
Flare-Ia	2.18 ± 0.10	2.95 ± 0.37	0.77 ± 0.38	2.11 ± 0.48	10.60	2.2σ
Interflare	2.07 ± 0.03	2.43 ± 0.07	0.36 ± 0.08	1.37 ± 0.12	16.20	3.0σ
Flare-Ib	2.05 ± 0.04	2.44 ± 0.13	0.39 ± 0.14	2.05 ± 0.36	9.00	1.9σ
Flare-Ic	1.99 ± 0.03	2.79 ± 0.19	0.79 ± 0.19	2.73 ± 0.64	41.40	$>5\sigma$
Postflare	2.08 ± 0.04	3.23 ± 0.27	1.15 ± 0.27	2.23 ± 0.12	27.60	4.3σ
Low	2.30 ± 0.02	3.10 ± 0.21	0.80 ± 0.21	3.00 ± 0.29	23.60	3.9σ

Note. All the columns represent the same parameters mentioned in Table 10.

c (cm s^{-1}) is the light velocity, θ_{jet} (degrees) is the viewing angle of the jet, and L_j (erg s^{-1}) is the total jet power. We considered a typical BLR cloud density value of $n_{c,0} = 10^{11}$ cm^{-3} (Netzer 2015). The estimated parameters are listed in Table 14. For BLR–jet interaction and cloud penetration to occur, Araudo et al. (2010) argued that the size of the BLR should be $R_{BLR} > z_{min}$. In this work, we find that the minimum interaction heights of the flares are larger than the size of the BLR ($R_{BLR} = 4.6 \times 10^{17}$ cm). Zacharias et al. (2017, 2019) have explained that the evolution of the long-term outburst in CTA 102 could be attributed to the ablation of a gas cloud penetrating into the relativistic jet, where such a gas cloud could likely originate from the atmosphere of a red-giant star or from material from a star-forming region that passed through the jet. However, our results do not appear to support the BLR–jet interaction mechanism for the short-timescale γ-ray flares from CTA 102. Shukla et al. (2018) surmised that the observed fast variability of CTA 102 may have resulted from the dissipation of magnetic islands or from protons in a collimated beam from the base of the jet encountering turbulent plasma at the end of the magnetic nozzle. A flare could also be derived from other physical mechanisms (Böttcher 2019a; Böttcher & Baring 2019b), such as from its geometric structure (bending or helical jets) or from a jet–star collision leading to the formation of a strong shock with subsequent particle acceleration, etc. Hence, further work is needed to investigate

Table 12
Fermi-LAT SEDs During the Different States of Flare-II, as Defined in Figure 4

PL					
Activity	Γ				
Low	2.30 ± 0.03			…	…
Plateau	2.11 ± 0.01			…	…
Flare-IIa	1.99 ± 0.01			…	…
Flare-IIb	2.02 ± 0.01			…	…
Flare-IIc	1.99 ± 0.01			…	…
Flare-IId	2.04 ± 0.01			…	…
Interflare	2.17 ± 0.01			…	…
Flare-IIe	2.07 ± 0.01			…	…
LP					
Activity	α	β		TS_{curve}	Curvature Significance
Low	2.20 ± 0.04	0.07 ± 0.02		23.6	2.7σ
Plateau	1.95 ± 0.02	0.09 ± 0.01		73.00	$>5\sigma$
Flare-IIa	1.87 ± 0.02	0.06 ± 0.01		64.00	$>5\sigma$
Flare-IIb	1.88 ± 0.02	0.08 ± 0.01		96.60	$>5\sigma$
Flare-IIc	1.84 ± 0.02	0.08 ± 0.01		145.80	$>5\sigma$
Flare-IId	1.91 ± 0.02	0.07 ± 0.01		70.60	$>5\sigma$
Interflare	2.02 ± 0.02	0.09 ± 0.01		86.40	$>5\sigma$
Flare-IIe	1.93 ± 0.02	0.08 ± 0.01		63.60	$>5\sigma$
PLEC					
Activity	Γ		E_c (GeV)	TS_{curve}	Curvature Significance
Low	2.23 ± 0.04		18.10 ± 8.55	12.20	1.8σ
Plateau	1.97 ± 0.02		9.90 ± 1.71	74.40	$>5\sigma$
Flare-IIa	1.87 ± 0.02		14.33 ± 2.18	89.00	$>5\sigma$
Flare-IIb	1.90 ± 0.02		12.78 ± 1.79	103.60	$>5\sigma$
Flare-IIc	1.86 ± 0.02		12.20 ± 1.39	165.60	$>5\sigma$
Flare-IId	1.93 ± 0.02		14.50 ± 2.36	74.40	$>5\sigma$
Interflare	2.04 ± 0.02		10.65 ± 1.85	68.00	$>5\sigma$
Flare-IIe	1.95 ± 0.02		12.48 ± 2.14	69.20	$>5\sigma$
BPL					
Activity	Γ_1	Γ_2	$\Delta\Gamma$	E_{break} (GeV)	TS_{curve}	Curvature Significance
Low	2.25 ± 0.03	2.84 ± 0.23	0.59 ± 0.23	3.00 ± 0.44	8.80	1.8σ
Plateau	2.03 ± 0.02	2.82 ± 0.13	0.79 ± 0.13	3.19 ± 0.30	64.80	$>5\sigma$
Flare-IIa	1.93 ± 0.01	3.14 ± 0.26	1.21 ± 0.26	6.82 ± 1.07	80.40	$>5\sigma$
Flare-IIb	1.97 ± 0.01	3.14 ± 0.23	1.17 ± 0.23	6.32 ± 0.91	87.80	$>5\sigma$
Flare-IIc	1.91 ± 0.01	2.80 ± 0.09	0.89 ± 0.09	3.92 ± 0.18	156.00	$>5\sigma$
Flare-IId	1.98 ± 0.02	2.96 ± 0.35	0.98 ± 0.35	5.35 ± 2.00	69.80	$>5\sigma$
Interflare	2.09 ± 0.02	2.95 ± 0.13	0.86 ± 0.13	3.02 ± 0.25	76.40	$>5\sigma$
Flare-IIe	2.01 ± 0.02	2.97 ± 0.16	0.96 ± 0.16	4.88 ± 0.32	90.90	$>5\sigma$

Note. All the columns represent the same parameters mentioned in Table 10.

the physical mechanism producing the flares of CTA 102 with multiband contemporaneous observations.

6. Summary

In this paper, we have studied the γ-ray flux and spectral variations of the FSRQ blazar CTA 102, using observational data collected by Fermi-LAT over 10 yr (2008–2018). The source displayed three major outburst periods (Flare-I, Flare-II, and Flare-III) with many substructures in the 7 day binned light curves. The variability and spectra of each individual outburst period were further studied to explore the triggering mechanism(s) and the physical properties of the emission regions. The main results are summarized as follows.

The source showed a rapid GeV flare of a symmetric temporal profile within the error bars, implying that the rise and decay timescales were dominated by the crossing time of radiation or due to disturbance by dense plasma blobs passing through the standing shock front in the jet region (Blandford & Königl 1979; Chatterjee et al. 2012). Moreover, some peaks also showed an asymmetric temporal profile in the 3 hr and 6 hr binned light curves, implying the fast injection of accelerated particles or escape from the emission region.

Table 13
Fermi-LAT SEDs During the Different States of Flare-III, as Defined in Figure 7

PL					
Activity	Γ				
Low 1	2.49 ± 0.05			⋯	⋯
Plateau	2.24 ± 0.02			⋯	⋯
Flare-IIIa	2.23 ± 0.04			⋯	⋯
Flare-IIIb	2.20 ± 0.02			⋯	⋯
Interflare	2.29 ± 0.03			⋯	⋯
Flare-IIIc	2.31 ± 0.02			⋯	⋯
Postflare	2.37 ± 0.04			⋯	⋯
Low 2	2.42 ± 0.06			⋯	⋯
LP					
Activity	α	β		TS_{curve}	Curvature Significance
Low 1	2.39 ± 0.06	0.11 ± 0.04		7.60	1.9σ
Plateau	2.10 ± 0.03	0.10 ± 0.02		46.40	$>5\sigma$
Flare-IIIa	2.09 ± 0.05	0.11 ± 0.03		15.20	3.2σ
Flare-IIIb	2.04 ± 0.03	0.12 ± 0.02		52.60	$>5\sigma$
Interflare	2.16 ± 0.04	0.11 ± 0.03		23.00	4.1σ
Flare-IIIc	2.19 ± 0.03	0.10 ± 0.02		26.80	4.5σ
Postflare	2.26 ± 0.06	0.10 ± 0.04		8.00	2.0σ
Low 2	2.32 ± 0.08	0.08 ± 0.05		3.40	$<1\sigma$
PLEC					
Activity	Γ		E_c (GeV)	TS_{curve}	Curvature Significance
Low 1	2.39 ± 0.07		8.27 ± 5.00	2.80	$<1\sigma$
Plateau	2.10 ± 0.03		8.36 ± 1.79	41.80	$>5\sigma$
Flare-IIIa	2.04 ± 0.06		5.46 ± 1.87	16.20	3.3σ
Flare-IIIb	2.03 ± 0.04		6.20 ± 1.36	43.80	$>5\sigma$
Interflare	2.14 ± 0.05		6.75 ± 2.21	18.40	3.6σ
Flare-IIIc	2.15 ± 0.04		5.98 ± 1.56	28.60	4.7σ
Postflare	2.21 ± 0.07		5.67 ± 2.37	9.20	2.2σ
Low 2	2.27 ± 0.10		6.07 ± 3.62	4.60	1.3σ
BPL					
Activity	Γ_1	Γ_2	$\Delta\Gamma$	E_{break} (GeV)	TS_{curve}	Curvature Significance
Low 1	2.34 ± 0.07	3.02 ± 0.24	0.68 ± 0.25	0.93 ± 0.20	9.20	1.9σ
Plateau	2.15 ± 0.03	2.74 ± 0.13	0.59 ± 0.14	1.78 ± 0.40	37.00	$>5\sigma$
Flare-IIIa	2.08 ± 0.06	2.54 ± 0.11	0.46 ± 0.13	0.82 ± 0.17	11.80	2.3σ
Flare-IIIb	2.11 ± 0.03	2.85 ± 0.19	0.75 ± 0.19	2.01 ± 0.47	35.40	$>5\sigma$
Interflare	2.23 ± 0.03	2.75 ± 0.19	0.53 ± 0.19	2.08 ± 0.31	9.80	2.0σ
Flare-IIIc	2.22 ± 0.03	3.13 ± 0.29	0.91 ± 0.30	2.01 ± 0.56	30.90	4.6σ
Postflare	2.28 ± 0.05	3.15 ± 0.36	0.87 ± 0.36	1.92 ± 0.39	9.60	2.0σ
Low 2	2.34 ± 0.07	3.10 ± 0.47	0.75 ± 0.47	2.05 ± 0.55	3.80	$<1\sigma$

Note. All the columns represent the same parameters mentioned in Table 10.

Based on the variability timescales of the GeV flares, various jet parameters (e.g., the Doppler factor, the emission region size, the angular size of the emission region, the location of the emission region, etc.) were constrained. These estimated parameters suggested that the location of the γ-ray emission region may lie in the inner jet upstream of the radio core (see Sections 5.1–5.3).

The γ-ray fluxes exhibited different distributions (see Section 3.4). The 1 day and 12 hr binned fluxes from Flare-I were in accordance with a log-normal distribution. Such a log-normal distribution of the observed flux may be explained by the relevant particle acceleration and diffusion processes (see, e.g., Shah et al. 2018; Sinha et al. 2018). The obtained shortest rise and decay timescales were 0.70 ± 0.05 hr from MJD 57,384.17 to 57,384.30 and 0.79 ± 0.27 hr from MJD 57,792.41 to 57,792.53, respectively. This short-timescale variability may have been triggered by magnetic field reconnection or shocks and interactions of the jet with external media (e.g., a BLR cloud or a star; see, e.g., Aharonian et al. 2017; Böttcher 2019a). In our work, the extreme γ-ray flare of CTA 102 is likely to have been caused by magnetic reconnection. Consequently, multiband synergistic observational data

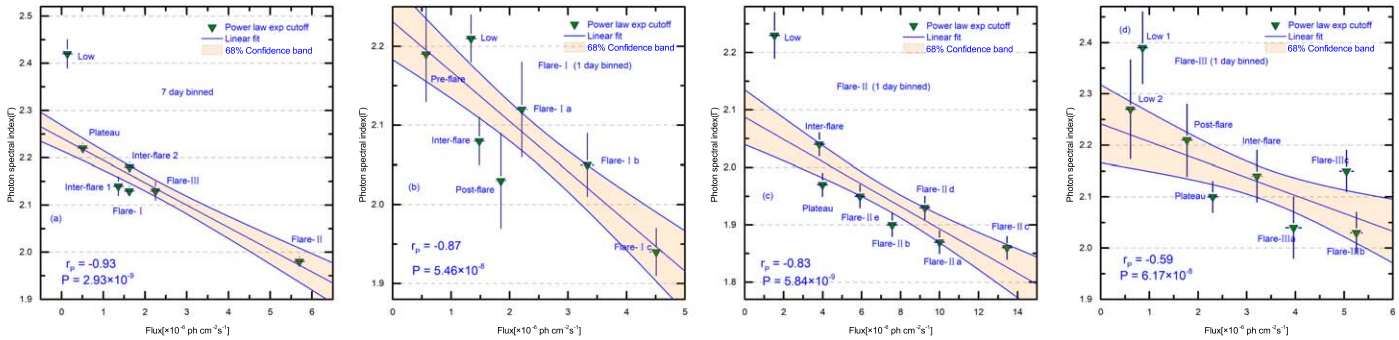

Figure 19. Spectral index as a function of flux for the different states. (a) The different states from the 7 day binned light curve (see Figure 1). (b) The different states from the 1 day binned light curve of Flare-I (see Figure 2(a)). (c) The different states from the 1 day binned light curve of Flare-II (see Figure 4(a)). (d) The different states from the 1 day binned light curve of Flare-III (see Figure 7(a)). All data points representing flux were derived using the PLEC model.

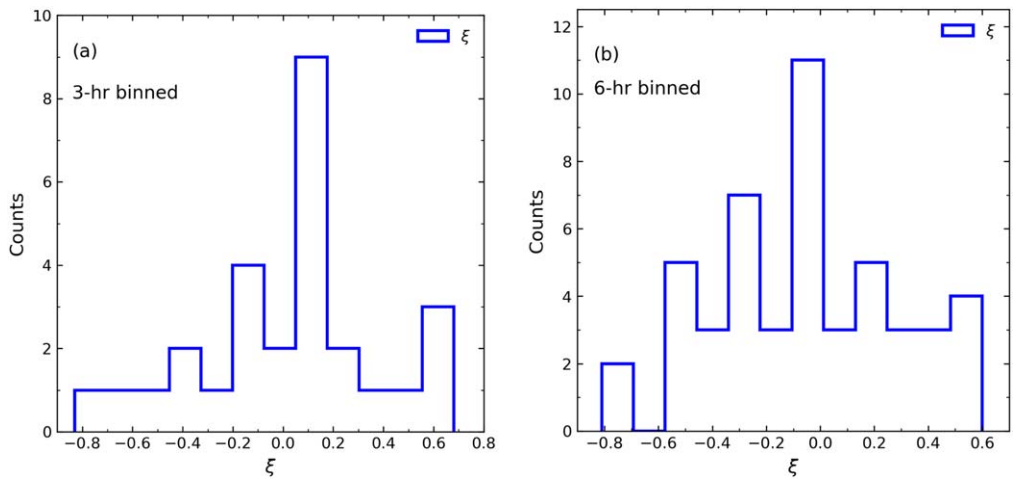

Figure 20. Histogram of the symmetry factor (ξ) from Table 2 and Tables 6–8, respectively.

Table 14
Calculated Parameters for All Flares

Flare	t_{var} (hr)	Cutoff Energy (GeV)	f_ϵ	δ_{min}	R	θ_{jet} (deg)	φ (μas)	L_j	$\Delta t_{max,h}$ (hr)	d_γ (pc)	d_γ (pc)	d_γ <(pc)	z_{min} (pc)
						Flare-I							
Flare-Ia	1.2 ± 0.2	7.0	0.7	14.6	0.9	3.9	0.1	3.2	3.8	0.01	0.004	4.73	0.10
Flare-Ib	2.2 ± 1.0	20.8	0.7	15.8	1.8	3.6	0.1	5.5	1.9	0.02	0.009	3.61	0.14
Flare-Ic	1.0 ± 0.5	6.6	0.7	14.8	0.8	3.8	0.1	8.3	3.8	0.01	0.004	4.79	0.16
						Flare-II							
Flare-IIa	1.2 ± 0.3	14.3	3.0	21.0	1.3	2.7	0.2	11.4	1.7	0.02	0.009	4.49	0.27
Flare-IIb	4.3 ± 1.0	12.8	2.0	15.5	3.6	3.7	0.1	14.8	9.4	0.04	0.018	7.80	0.22
Flare-IIc	2.3 ± 0.8	12.2	4.5	19.5	2.4	2.9	0.1	17.7	3.1	0.03	0.015	5.67	0.31
Flare-IId	6.7 ± 3.5	14.5	4.8	17.0	6.0	3.4	0.1	14.8	38.4	0.07	0.033	17.38	0.25
Flare-IIe	1.0 ± 0.7	12.5	2.0	19.7	1.0	2.9	0.1	6.6	14.9	0.01	0.007	12.50	0.19
						Flare-III							
Flare-IIIc	1.2 ± 1.0	6.0	3.5	18.6	1.2	3.1	0.1	4.3	5.5	0.01	0.007	7.22	0.15

Note. Here, f_ϵ is the X-ray flux in the 2–10 keV energy band in units of 10^{-11} erg s^{-1}, which is based on the results of Zacharias et al. (2019) and the observations made by the Boston University Blazar Group (http://www.bu.edu/blazars/VLBAproject.html). R is the size of the emission region in units of 10^{15} cm, while L_j is the total jet power in units of 10^{47} erg s^{-1}.

would be needed to investigate the physical mechanism of the rapid flaring activity of CTA 102 in more detail.

The γ-ray spectra from the different states seen in the 1 day and 7 day binned light curves were fitted with four different equations (PL, LP, PLEC, and BPL). The source exhibited a significant GeV spectral cutoff/break. The ranges of the cutoff/break energies found with the PLEC and BPL models were from (5.46 ± 1.87) GeV to (20.78 ± 5.52) GeV and from

Table 15
Results of the Variability Timescale of Doubling/Halving by Scanning the 3 hr Binned Light Curves for Each Flare

$T_{start}(t_1)$ (MJD)	Flux Start (F_1) (10^{-6} ph cm^{-2} s^{-1})	$T_{stop}(t_2)$ (MJD)	Flux Stop (F_2) (10^{-6} ph cm^{-2} s^{-1})	τ (hr)	τ_z (hr)	Rise/Decay
			Flare-Ia			
57,384.17	3.53 ± 0.69	57,384.30	15.07 ± 1.35	1.43 ± 0.11	0.70 ± 0.05	R
57,384.30	15.07 ± 1.35	57,384.42	6.00 ± 1.06	−2.26 ± 0.21	−1.11 ± 0.10	D
57,384.92	3.49 ± 0.82	57,385.05	7.09 ± 1.17	2.94 ± 0.29	1.44 ± 0.14	R
			Flare-Ib			
57,423.55	4.07 ± 1.69	57,423.67	1.32 ± 0.64	−1.85 ± 0.11	−0.91 ± 0.06	D
57,425.67	6.00 ± 1.58	57,425.80	2.22 ± 0.69	−2.09 ± 0.10	−1.03 ± 0.05	D
57,426.42	2.25 ± 0.63	57,426.55	7.78 ± 2.04	1.68 ± 0.02	0.82 ± 0.01	R
			Flare-Ic			
57,431.67	4.13 ± 1.39	57,431.80	1.54 ± 0.60	−2.11 ± 0.11	−1.04 ± 0.06	D
57,432.17	3.64 ± 0.80	57,432.30	1.50 ± 0.56	−2.35 ± 0.41	−1.15 ± 0.20	D
57,435.05	4.58 ± 0.95	57,435.17	2.09 ± 0.63	−2.65 ± 0.32	−1.30 ± 0.16	D
57,436.30	8.22 ± 1.16	57,436.42	2.89 ± 1.00	−1.99 ± 0.39	−0.98 ± 0.19	D
57,437.92	3.09 ± 0.69	57,438.05	6.64 ± 0.96	2.72 ± 0.28	1.34 ± 0.14	R
57,438.30	7.77 ± 1.19	57,438.42	15.83 ± 1.95	2.92 ± 0.12	1.43 ± 0.06	R
57,438.42	15.83 ± 1.95	57,438.55	5.12 ± 1.80	−1.84 ± 0.37	−0.90 ± 0.18	D
57,438.92	4.36 ± 0.86	57,439.05	9.76 ± 1.18	2.58 ± 0.24	1.27 ± 0.12	R
57,439.80	10.42 ± 2.29	57,439.92	4.91 ± 0.90	−2.76 ± 0.13	−1.36 ± 0.07	D
57,440.67	1.53 ± 0.74	57,440.80	4.44 ± 0.85	1.95 ± 0.54	0.96 ± 0.26	R
57,441.67	5.95 ± 1.63	57,441.80	2.68 ± 0.81	−2.60 ± 0.09	−1.28 ± 0.05	D
57,442.42	3.49 ± 0.92	57,442.55	9.40 ± 2.20	2.10 ± 0.06	1.03 ± 0.03	R
57,443.17	4.26 ± 0.86	57,443.30	1.32 ± 0.54	−1.78 ± 0.31	−0.87 ± 0.15	D
57,445.17	3.15 ± 0.81	57,445.30	1.37 ± 0.60	−2.49 ± 0.54	−1.22 ± 0.27	D
			Flare-IIa/b/c/d			
57,735.53	3.73 ± 0.96	57,735.66	10.10 ± 1.69	2.09 ± 0.19	1.03 ± 0.09	R
57,757.66	6.34 ± 1.42	57,757.78	13.41 ± 1.84	2.77 ± 0.32	1.36 ± 0.16	R
57,758.66	11.27 ± 1.51	57,758.78	5.34 ± 2.41	−2.79 ± 1.18	−1.37 ± 0.58	D
57,758.78	5.34 ± 2.41	57,758.91	14.88 ± 1.62	2.03 ± 0.68	1.00 ± 0.33	R
			Flare-IIe			
57,789.66	1.74 ± 0.81	57,789.78	4.08 ± 1.26	2.44 ± 0.45	1.20 ± 0.22	R
57,790.28	7.13 ± 1.28	57,790.41	2.73 ± 1.53	−2.16 ± 0.86	−1.06 ± 0.42	D
57,792.41	6.52 ± 1.15	57,792.53	1.78 ± 1.12	−1.60 ± 0.56	−0.79 ± 0.27	D
57,792.53	1.78 ± 1.12	57,792.66	6.23 ± 1.61	1.66 ± 0.49	0.82 ± 0.24	R
57,797.16	4.14 ± 0.94	57,797.28	1.81 ± 0.85	−2.51 ± 0.74	−1.23 ± 0.36	D
57,797.28	1.81 ± 0.85	57,797.41	6.23 ± 1.20	1.68 ± 0.38	0.83 ± 0.19	R
57,798.78	9.38 ± 1.35	57,798.91	4.68 ± 0.84	−3.00 ± 0.15	−1.47 ± 0.08	D
57,801.03	2.52 ± 0.96	57,801.16	6.55 ± 1.10	2.18 ± 0.49	1.07 ± 0.24	R
57,801.28	7.97 ± 1.12	57,801.41	3.35 ± 1.26	−2.40 ± 0.65	−1.18 ± 0.32	D
57,802.66	5.22 ± 1.72	57,802.78	2.14 ± 0.92	−2.34 ± 0.26	−1.15 ± 0.13	D
57,803.28	1.69 ± 0.58	57,803.41	4.21 ± 1.74	2.28 ± 0.17	1.12 ± 0.09	R
57,804.16	1.38 ± 0.59	57,804.28	2.94 ± 0.83	2.74 ± 0.53	1.34 ± 0.26	R
			Flare-IIIa/b			
58,117.53	4.92 ± 1.26	58,117.66	1.74 ± 0.89	−2.00 ± 0.49	−0.98 ± 0.24	D
58,117.66	1.74 ± 0.89	58,117.78	4.10 ± 1.38	2.42 ± 0.50	1.19 ± 0.24	R
58,118.66	3.68 ± 1.15	58,118.78	9.76 ± 3.39	2.13 ± 0.08	1.05 ± 0.04	R
58,118.78	9.76 ± 3.39	58,118.91	3.13 ± 0.91	−1.83 ± 0.09	−0.90 ± 0.04	D
58,121.53	5.74 ± 1.24	58,121.66	1.84 ± 0.97	−1.83 ± 0.50	−0.90 ± 0.25	D
58,125.53	3.28 ± 1.13	58,125.66	8.38 ± 1.42	2.22 ± 0.41	1.09 ± 0.20	R
58,127.66	5.69 ± 1.64	58,127.78	2.77 ± 0.97	−2.88 ± 0.25	−1.41 ± 0.12	D
			Flare-IIIc			
58,141.41	1.71 ± 0.71	58,141.53	4.27 ± 1.29	2.28 ± 0.28	1.12 ± 0.14	R
58,141.78	2.18 ± 0.76	58,141.91	5.59 ± 1.38	2.21 ± 0.24	1.08 ± 0.12	R
58,142.53	6.71 ± 1.79	58,142.66	2.59 ± 1.20	−2.18 ± 0.45	−1.07 ± 0.22	D
58,142.66	2.59 ± 1.20	58,142.78	7.30 ± 1.32	2.01 ± 0.55	0.99 ± 0.27	R
58,147.41	2.52 ± 0.83	58,147.53	5.53 ± 1.08	2.65 ± 0.45	1.30 ± 0.22	R

Table 15
(Continued)

$T_{start}(t_1)$ (MJD)	Flux Start (F_1) (10^{-6} ph cm^{-2} s^{-1})	$T_{stop}(t_2)$ (MJD)	Flux Stop (F_2) (10^{-6} ph cm^{-2} s^{-1})	τ (hr)	τ_z (hr)	Rise/Decay
58,148.53	5.39 ± 1.12	58,148.66	2.13 ± 0.81	-2.24 ± 0.42	-1.10 ± 0.20	D
58,148.66	2.13 ± 0.81	58,148.78	6.74 ± 1.20	1.81 ± 0.32	0.89 ± 0.16	R
58,150.16	1.70 ± 0.48	58,150.28	4.40 ± 1.13	2.18 ± 0.06	1.07 ± 0.03	R
58,150.91	3.92 ± 0.95	58,151.03	1.39 ± 0.58	-2.01 ± 0.34	-0.99 ± 0.17	D
58,151.28	2.45 ± 0.87	58,151.41	5.63 ± 1.07	2.49 ± 0.50	1.22 ± 0.24	R

Note. Here, τ (Column (5)) is the characteristic timescale, which was estimated using Equation (9). The parameter τ_z (Column (6)) is the redshift-corrected doubling/halving timescale, namely, $\tau_z = \tau/(1+z)$. The uncertainty of the timescale was calculated by propagating the uncertainties in the flux and time values through Equation (9). Column 7 (Rise/Decay) suggests whether the variability event represents an increase (Rise) or decrease (Decay) in the flux for a given interval between T_{start} (Column (1)) and T_{stop} (Column (3)).

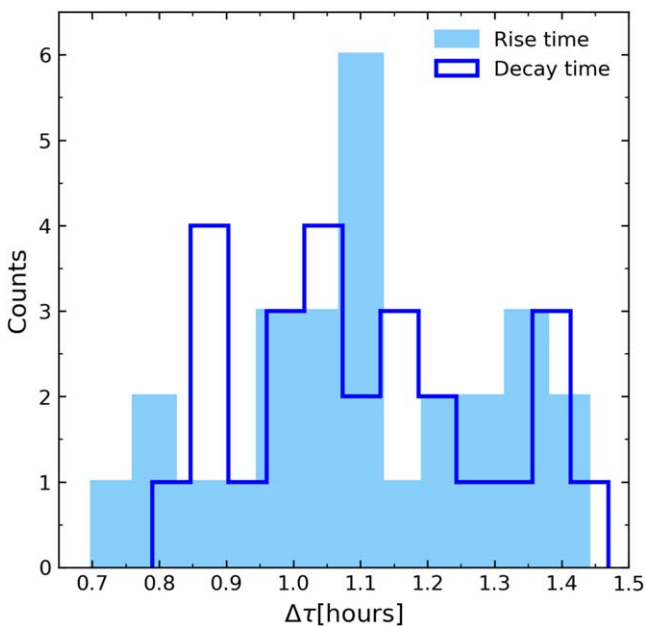

Figure 21. Histogram of the rise and decay timescales from Table 15. They are distributed about means of 1.10 ± 0.03 hr and 1.11 ± 0.04 hr, respectively.

(0.82 ± 0.17) GeV to (8.00 ± 0.59) GeV, respectively. We also find that the best-fitting form for the flare period is the PLEC function, which is consistent with the result of Ballet et al. (2020; see the Fermi Large Area Telescope Fourth Source Catalog, Data Release 2). The source also displayed "harder-when-brighter" behavior during the different activity states.

In CTA 102, the characteristics of its flux variability and spectral evolution seem to support the idea that the γ-ray emission regions vary from one flare to another, although, in general, the distance of the γ-ray emission region is located upstream of the radio core. Further contemporaneous multiband observations are needed to identify the origin of such ultrafast γ-ray variability and put a stronger constraint on the various jet parameters.

We thank the anonymous referee for the insightful comments, which have significantly improved our manuscript. This work was partially supported by the National Key Research and Development Program (2018YFA0404204), the National Science Foundation of China (grants U1531131 and 11433004), the Science Foundation of Yunnan Province (No. 2018FA004), the Yunnan High-level personnel training support program, the University Key Laboratory of Information and Communication on Security Backup and Recovery in Yunnan Province, the National Science Foundation of China (grant 12003026 and 11903028), the Basic Research Program of Yunnan 202001AU070070, and the Research Foundation of the Education Bureau of Yunnan Province, China (grant No. 2021J0715). N.D. acknowledges financial support from the National Natural Science Foundation of China (No. 12103022) and the Special Basic Cooperative Research Programs of the Yunnan Provincial Undergraduate Universities' Association (NO. 202101BA070001-043). P.K. acknowledges the ARIES Aryabhatta Fellowship (AO/A-PDF/770).

Appendix A
Identifying the 3 hr Binned Light Curves

Figure A1 presents the 3 hr binned light curves of flares a–c from the Flare-I period, flares a–e from the Flare-II period, and flare c from the Flare-III period, which are described in Sections 3.3.1, 3.3.2, and 3.3.3. All peaks are identified by the BB algorithm, with the false alarm rate parameter $p_0 = 0.05$.

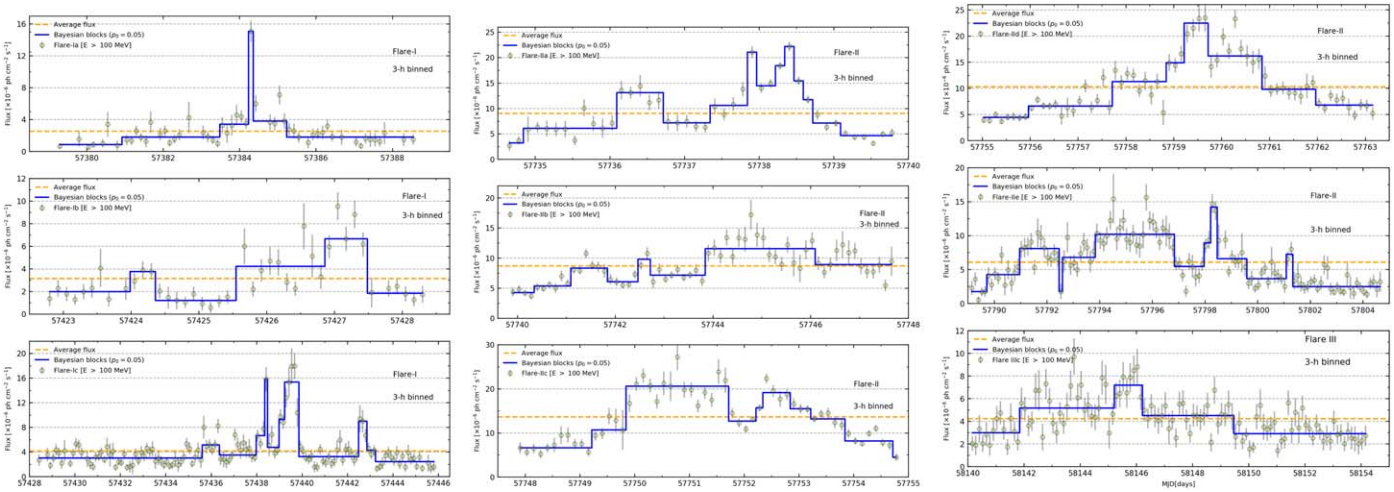

Figure A1. The 3 hr binned light curves of flares a–c from the Flare-I period (see Figure 2), flares a–e from the Flare-II period (see Figure 4), and flare c from Flare-III period (see Figures 4 and 7). The peaks are identified by the BB algorithm, with the false alarm rate parameter $p_0 = 0.05$.

Appendix B
Identifying the 6 hr Binned Light Curves

Figures B1 and B2 present the 6 hr binned light curves of flares a–c from the Flare-I period, flares a–e from the Flare-II period, and flare c from the Flare-III period in the 0.1–1 GeV, 1–300 GeV, and 0.1–300 GeV energy bands. All peaks are identified by the BB algorithm, with the false alarm rate parameter $p_0 = 0.05$.

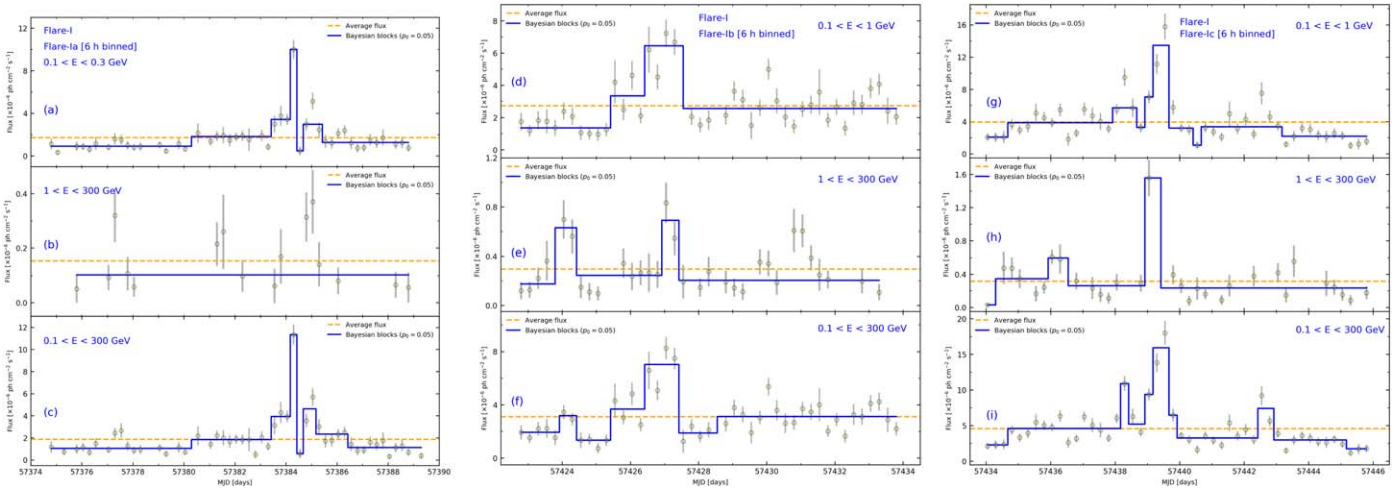

Figure B1. The 6 hr binned light curves of flares a–c from the Flare-I period and flare c from the Flare-III period. All peaks are identified by the BB algorithm, with the false alarm rate parameter $p_0 = 0.05$.

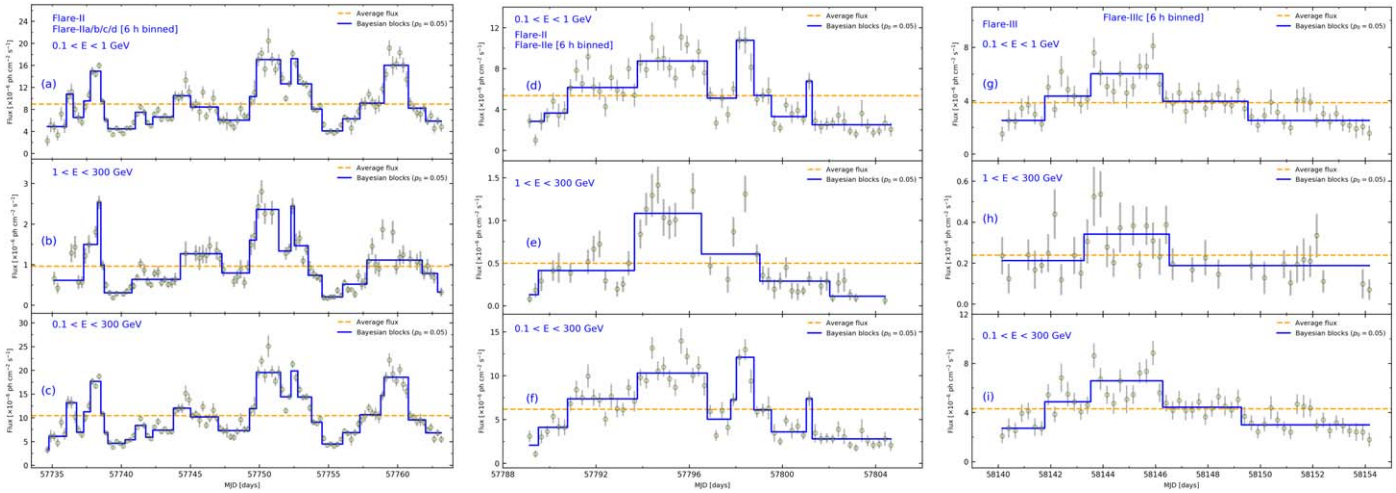

Figure B2. The 6 hr binned light curves of flares a–e from the Flare-II period. All peaks are identified by the BB algorithm, with the false alarm rate parameter $p_0 = 0.05$.

ORCID iDs

Nan Ding https://orcid.org/0000-0003-1028-8733
Celine Chidiac https://orcid.org/0000-0001-5720-5419
Pankaj Kushwaha https://orcid.org/0000-0001-6890-2236
Zahir Shah https://orcid.org/0000-0003-1458-4396
Xiongbang Yang https://orcid.org/0000-0002-1496-3209
Zejun Jiang https://orcid.org/0000-0002-4705-2479
Wei Zeng https://orcid.org/0000-0002-4144-5378
Benzhong Dai https://orcid.org/0000-0001-7908-4996

References

Abdo, A. A., Ackermann, M., Ajello, M., et al. 2010a, ApJ, 722, 520
Abdo, A. A., Ackermann, M., Agudo, I., et al. 2010b, ApJ, 721, 1425
Abeysekara, A. U., Archambault, S., Archer, A., et al. 2017, ApJ, 834, 2
Ackermann, M., Ajello, M., Baldini, L., et al. 2010, ApJ, 721, 1383
Ackermann, M., Anantua, R., Asano, K., et al. 2016, ApJL, 824, L20
Agudo, I., Marscher, A. P., Jorstad, S. G., et al. 2011, ApJL, 735, L10
Algaba, J. C., Nakamura, M., Asada, K., et al. 2017, ApJ, 834, 65
Aharonian, F. A., Barkov, M. V., & Khangulyan, D. 2017, ApJ, 841, 61
Ait Benkhali, F., Hofmann, W., Rieger, F. M., et al. 2019, A&A, 634, A120
Araudo, A. T., Bosch-Ramon, V., & Romero, G. E. 2009, A&A, 503, 673
Araudo, A. T., Bosch-Ramon, V., & Romero, G. E. 2010, A&A, 522, A97
Araudo, A. T., Bosch-Ramon, V., & Romero, G. E. 2013, MNRAS, 436, 3626
Arévalo, P., & Uttley, P. 2006, MNRAS, 367, 801
Atwood, W. B., Abdo, A. A., Ackermann, M., et al. 2009, ApJ, 697, 1071
Ballet, J., Burnett, T. H., Digel, S. W., & Lott, B. 2020, arXiv:2005.11208
Baghmanyan, V., Gasparyan, S., & Sahakyan, N. 2017, ApJ, 848, 111
Barkov, M. V., Aharonian, F. A., Bogovalov, S. V., et al. 2012, ApJ, 749, 119
Blandford, R. D., & Königl, A. 1979, ApJ, 232, 34
Böttcher, M., & Chiang, J. 2002, ApJ, 581, 127
Böttcher, M., & Dermer, C. D. 2010, ApJ, 711, 445
Böttcher, M., Reimer, A., Sweeney, K., et al. 2013, ApJ, 768, 54
Böttcher, M. 2019a, Galax, 7, 20
Böttcher, M., & Baring, M. G. 2019b, ApJ, 887, 133
Bodo, G., & Tavecchio, F. 2018, A&A, 609, A122
Britto, R. J., Bottacini, E., Lott, B., et al. 2016, ApJ, 830, 162
Burns, E., Tohuvavohu, A., Bellovary, J. M., et al. 2019, BAAS, 51, 250
Cao, G., & Wang, J. C. 2013, PASJ, 65, 109
Cao, G., & Wang, J. C. 2014, ApJ, 783, 108
Cao, G., Yang, C., Yang, J., & Wang, J. 2020, PASJ, 72, 20
Carrasco, L., Luna, A., Porras, A., et al. 2012, ATel, 4442, 1
Casadio, C., Gómez, J. L., Jorstad, S. G., et al. 2015, ApJ, 813, 51
Casadio, C., Marscher, A. P., Jorstad, S. G., et al. 2019, A&A, 622, A158
Cerruti, M., Zech, A., Boisson, C., & Inoue, S. 2015, MNRAS, 448, 910
Cerruti, M., Zech, A., & Boisson, C. 2019, MNRAS, 483, L12
Chatterjee, R., Bailyn, C. D., Bonning, E. W., et al. 2012, ApJ, 749, 191
Chavushyan, V., Patiño-Álvarez, V. M., Amaya-Almazán, R. A., & Carrasco, L. 2020, ApJ, 891, 68
Ciprini, S., & Verrecchia, F. 2016, ATel, 9841, 1
Das, A. K., Prince, R., & Gupta, N. 2020, ApJS, 248, 8
D'Ammando, F., Raiteri, C. M., Villata, M., et al. 2019, MNRAS, 490, 5300
De, K., Hankins, M., Kasliwal, M. M., et al. 2019, ATel, 13051, 1
de la Cita, V. M., Bosch-Ramon, V., Paredes-Fortuny, X., et al. 2016, A&A, 591, A15
del Palacio, S., V. Bosch-Ramon, V., & Romero, G. E. 2019, A&A, 623, A101
Dermer, C. D., Cerruti, M., Lott, B., et al. 2014, ApJ, 782, 82
Ding, N., Zhang, X., Xiong, D. R., & Zhang, H. J. 2017, MNRAS, 464, 599
Ding, N., Gu, Q. S., Geng, X. F., et al. 2019, ApJ, 881, 125
Dondi, L., & Ghisellini, G. 1995, MNRAS, 273, 583
Dotson, A., Georganopoulos, M., Kazanas, D., et al. 2012, ApJL, 758, L15
Finke, J. D., Dermer, C. D., & Böttcher, M. 2008, ApJ, 686, 181
Foschini, L., Ghisellini, G., Tavecchio, F., et al. 2011, A&A, 530, A77
Fromm, C. M., Ros, E., Perucho, M., et al. 2013a, A&A, 551, A32
Fromm, C. M., Ros, E., Perucho, M., et al. 2013b, A&A, 557, A105
Gasparyan, S., Sahakyan, N., Baghmanyan, V., et al. 2018, ApJ, 863, 114
Geng, X., Zeng, W., Rani, B., et al. 2020, ApJ, 904, 67
Giannios, D., Uzdensky, D. A., & Begelman, M. C. 2009, MNRAS, 395, L29
Giannios, D. 2013, MNRAS, 431, 355
Guo, F., Li, H., Daughton, W., et al. 2014, PhRvL, 113, 155005
Guo, F., Liu, Y. H., Daughton, W., & Li, H. 2015, ApJ, 806, 167
Hayashida, M., Nalewajko, K., Madejski, G. M., et al. 2015, ApJ, 807, 79
Jorstad, S. G., Marscher, A. P., Lister, A. P., et al. 2005, AJ, 130, 1418
Jorstad, S. G., Marscher, A. P., Morozova, D. A., et al. 2017, ApJ, 846, 98
Joshi, M., & Böttcher, M. 2011, ApJ, 727, 21
Joshi, M., Marscher, A. P., & Böttcher, M. 2014, ApJ, 785, 132
Kaur, N., & Baliyan, K. S. 2018, A&A, 617, A59
Khatoon, R., Shah, Z., Misra, R., & Gogo, R. 2020, MNRAS, 491, 1934
Kirk, J. G., Rieger, F., & Mastichiadis, A. 1998, A&A, 333, 452
Kirk, J. G., & Mastichiadis, A. 1999, APh, 11, 45
Komissarov, S. S. 2003, MNRAS, 341, 717
Kushwaha, P., Sahayanathan, S., Lekshmi, R., et al. 2014a, MNRAS, 442, 131
Kushwaha, P., Singh, K. P., & Sahayanathan, S. 2014b, ApJ, 796, 61
Kushwaha, P., Chandra, S., Misra, R., et al. 2016, ApJL, 822, L13
Kushwaha, P., Sinha, A., Misra, R., et al. 2017, ApJ, 849, 138
Larionov, V. M., Blinov, D., & Jorstad, S. 2012, ATel, 4397, 1
Larionov, V. M., Villata, M., Raiteri, C. M., et al. 2016, MNRAS, 461, 3047
Lewis, T. R., Finke, J. D., & Becker, P. A. 2018, ApJ, 853, 6
Lewis, T. R., Finke, J. D., & Becker, P. A. 2019, ApJ, 884, 116
Li, X. F., Mohan, P., An, T., et al. 2018, ApJ, 854, 17
Li, H., & Kusunose, M. 2000, ApJ, 536, 729
Lyubarsky, Y. E. 2005, MNRAS, 358, 113
Lyubarskii, Yu. E. 1997, MNRAS, 292, 679
MAGIC Collaboration, Ahnen, M. L., Ansoldi, S., et al. 2018, A&A, 619, A45
Malmrose, M. P., Marscher, A. P., Jorstad, S. G., et al. 2011, ApJ, 732, 116
Marscher, A. P., Marshall, F. E., Mushotzky, R. F., et al. 1979, ApJ, 233, 498
Meyer, M., Scargle, J. D., & Blandford, R. D. 2019, ApJ, 877, 39
Moore, R. L., & Stockman, H. S. 1981, ApJ, 243, 60
Morris, P. J., Potter, W. J., & Cotter, G. 2019, MNRAS, 486, 1548
Murase, K., & Bartos, I. 2019, ARNPS, 69, 477
Nalewajko, K., Begelman, M. C., & Sikora, M. 2014, ApJ, 789, 161

Netzer, H. 2015, ARA&A, 53, 365
Nolan, P. L., Bertsch, D. L., Fichtel, C. E., et al. 1993, ApJ, 414, 82
Nolan, P. L., Abdo, A. A., Ackermann, M., et al. 2012, ApJS, 119, 31
Ojha, R., Carpenter, B., & D'Ammand, F. 2017, ATel, 9924, 1
Orienti, M., D'Ammando, F., Giroletti, M., et al. 2020, MNRAS, 491, 858
Padovani, P., Alexander, D. M., Assef, R. J., et al. 2017, A&ARv, 25, 2
Paliya, V. S. 2015a, ApJL, 808, L48
Paliya, V. S. 2015b, ApJ, 804, 74
Petropoulou, M., Giannios, D., & Sironi, L. 2016, MNRAS, 462, 3325
Prince, R., Majumdar, P., & Gupta, N. 2017, ApJ, 844, 62
Prince, R., Raman, G., Hahn, J., et al. 2018, ApJ, 866, 16
Pushkarev, A. B., Hovatta, T., Kovalev, Y. Y., et al. 2012, A&A, 545, A113
Raiteri, C. M., Villata, M., Acosta-Pulido, J. A., et al. 2017, Natur, 552, 374
Rani, B., Krichbaum, T. P., Fuhrmann, L., et al. 2013a, A&A, 552, A11
Rani, B., Lott, B., Krichbaum, T. P., et al. 2013b, A&A, 557, A71
Rani, B., Petropoulou, M., Zhang, H., et al. 2019, BAAS, 51, 92
Razali, N. M., & Wah, Y. B. 2011, Journal of Statistical Modeling and Analytics, 2, 21
Roy, N., Chatterjee, R., Joshi, M., et al. 2019, MNRAS, 482, 743
Sahakyan, N. 2019, A&A, 635, A25
Scargle, J. D., Norris, J. P., Jackson, B., et al. 2013, ApJ, 764, 167
Shah, Z., Mankuzhiyil, N., Sinha, A., et al. 2018, RAA, 18, 141
Shapiro, S. S., & Wilk, M. B. 1965, Biometrika, 52, 591
Shukla, A., Mannheim, K., Patel, S. R., et al. 2018, ApJL, 854, L26
Shukla, A., & Mannheim, K. 2020, NatCo, 11, 4176
Sikora, M., Błażejowski, M., Begelman, M. C., et al. 2001, ApJ, 554, 1
Sinha, A., Khatoon, R., Misra, R., et al. 2018, MNRAS, 480, L116
Sironi, L., Petropoulou, M., & Giannios, D. 2015, MNRAS, 450, 183
Svensson, R. 1987, MNRAS, 227, 403
Tanaka, Y. T., Stawarz, L., Thompson, D. J., et al. 2011, ApJ, 733, 19
Tanihata, C., Urry, C. M., Takahashi, T., et al. 2001, ApJ, 563, 569
Urry, C. M., & Padovani, P. 1995, PASP, 107, 803
Wang, Y. J., Xue, Y. Q., Zhu, S. F., et al. 2018, ApJ, 867, 68
Wang, Y. J., Zhu, S. F., Xue, Y. Q., et al. 2019, ApJ, 885, 8
Wierzcholska, A., & Siejkowski, H. 2016, MNRAS, 458, 2350
Xiong, D. R., & Zhang, X. 2014, MNRAS, 441, 3375
Xue, R., Liu, R. Y., Wang, X. Y., Yan, H. R., & Böttcher, M. 2019, ApJ, 871, 81
Zacharias, M., Böttcher, M., Jankowsky, F., et al. 2017, ApJ, 851, 72
Zacharias, M., Böttcher, M., Jankowsky, F., et al. 2019, ApJ, 871, 19
Zamaninasab, M., Clausen-Brown, E., Savolainen, T., et al. 2014, Natur, 510, 126
Zhang, J., Zhang, H. M., Gan, Y. Y., et al. 2020, ApJ, 559, 2
Zhu, S. F., Xue, Y. Q., Brandt, W. N., Cui, W., & Wang, Y. J. 2018, ApJ, 853, 34